
A Comparison of Hypersonic Vehicle Flight and Prediction Results

Kenneth W. Iliff and Mary F. Shafer

October 1995



National Aeronautics and
Space Administration

A Comparison of Hypersonic Vehicle Flight and Prediction Results

Kenneth W. Iliff and Mary F. Shafer
NASA Dryden Flight Research Center
Edwards, California

1995



National Aeronautics and
Space Administration

Dryden Flight Research Center
Edwards, California 93523-0273

A COMPARISON OF HYPERSONIC FLIGHT AND PREDICTION RESULTS

Kenneth W. Iliff* and Mary F. Shafer**
 NASA Dryden Flight Research Facility
 P. O. Box 273
 Edwards, California 93523-0273

Abstract

Aerodynamic and aerothermodynamic comparisons between flight and ground test for four hypersonic vehicles are discussed. The four vehicles are the X-15, the Reentry F, the Sandia Energetic Reentry Vehicle Experiment (SWERVE), and the Space Shuttle. The comparisons are taken from papers published by researchers active in the various programs. Aerodynamic comparisons include reaction control jet interaction on the Space Shuttle. Various forms of heating including catalytic, boundary layer, shock interaction and interference, and vortex impingement are compared. Predictions were significantly exceeded for the heating caused by vortex impingement (on the Space Shuttle OMS pods) and for heating caused by shock interaction and interference on the X-15 and the Space Shuttle. Predictions of boundary-layer state were in error on the X-15, the SWERVE, and the Space Shuttle vehicles.

Nomenclature

Acronyms

ACIP	Aerodynamic Coefficient Instrumentation Package
ADDB	Aerodynamic design data book for the orbiter vehicle ¹
CFD	computational fluid dynamics
CP	center of pressure
EST	estimated
GELMA	General Electric low mass addition

HRSI	high-temperature reusable surface insulation
IMU	inertial measurement unit
NASP	National Aero-Space Plane
NOM	nominal
OEX	orbiter experiments
OI	operational instrumentation
OMS	orbital maneuvering system
PNS	parabolized Navier-Stokes
POPU	push-over-pull-up or pull-up-push-over
RCC	reinforced carbon-carbon
RCG	reaction-cured glass
RCS	reaction control system
SHTNEQ	viscous-shock-layer code
STS	Space Transportation System, prefix for flight number
SWERVE	Sandia Winged Energized Reentry Vehicle Experiment
TPS	thermal protection system
T/C	thermocouple

Symbols

a_n	normal acceleration, g
C'_{∞}	free-stream proportionality factor for the linear viscosity-temperature relationship
C_m	coefficient of pitching moment
C_N	coefficient of normal force
h	altitude, ft
h	heat transfer coefficient, BTU/ft ² -sec-deg (Fahrenheit or Rankine)
h_o	Undisturbed heat transfer coefficient, BTU/ft ² -sec-deg (Rankine)

*Senior Staff Scientist. Fellow, AIAA.

**Aerospace Engineer. Associate Fellow, AIAA.

Copyright ©1993 by the American Institute of Aeronautics and Astronautics, Inc. No copyright is asserted in the United States under Title 17, U.S. Code. The U.S. Government has a royalty-free license to exercise all rights under the copyright claimed herein for Governmental purposes. All other rights are reserved by the copyright owner.

K	height difference relative to adjacent tiles, in.
k_w	surface catalytic recombination rate constant, cm/sec
k_{wN}	k_w for nitrogen, cm/sec
k_{wO}	k_w for oxygen, cm/sec
L	length of orbiter, 32.77 m, 107.75 ft, or 1295 in.
L_{YJ}	rolling moment due to yaw jet, ft-lbf per jet
M_∞	freestream Mach number
$M_\infty/\sqrt{R_\infty}$	viscous interaction parameter
\dot{M}_j/\dot{M}_∞	jet-to-freestream mass flow ratio
M_{MAX}	maximum Mach number
$N_{St,l}$	local incompressible Stanton number
$N_{Re,l}$	local Reynolds number
q	convective heat-transfer rate, Btu/ft ² -sec
\dot{q}	pitch rate, deg/sec
q_c	convective heat-transfer rate, Btu/ft ² -sec
\dot{q}	heat-transfer rate, kW/m ²
Re	Reynolds number
Re_s	Reynolds number based on distance to transition
Re_∞	freestream Reynolds number
Re_k	Reynolds number at top of misaligned tiles
$R_{NS,L}$	Reynolds number evaluated behind a normal shock based on orbiter characteristic length
$R_{NS,L}^{0.2}$	$R_{NS,L}$ at $X/L = 0.2$
S	surface length, in.
St	Stanton number
s/L	side fuselage thermocouple location
T	temperature, °F or °R
\bar{T}	normalized surface temperature
T_{re}	radiation equilibrium temperature
T_w	wall temperature, °R
t	time, sec
U_∞	freestream velocity, km/sec
\bar{V}'_∞	viscous interaction parameter, $M_\infty \sqrt{\frac{C_{fa}}{Re}}$
X	axial coordinate, in.
X, x	axial distance from nose of orbiter, m

$X/L, x/L$	nondimensional body length
X_{CP}/LB	center of pressure location, fraction of body length
Y	spanwise coordinate, in.
α	angle of attack, deg
β	angle of sideslip, deg
δ	control surface deflection
δ_a	aileron (differential elevon) deflection, deg
δ_e	elevator (symmetric elevon) deflection, deg
δ_{TRIM}	trimmed control surface deflection, deg
ϵ	emissivity
ϵ_{TH}	total hemispherical emittance
θ	pitch angle, deg
ρ_∞	freestream density, kg/m ³
ϕ	angular ray on cone surface, deg

Introduction

There is continued interest in advancing the understanding of aerodynamic phenomena as seen in the comparison of flight and ground test data. These continuing comparisons have caused the steady advancement of aerodynamics (new phenomenology and modified theory) by forcing "agreement" between ground and flight results. This has resulted in more advanced flight vehicles with ever-increasing economy, safety, and overall aircraft performance. We demonstrated manned hypersonic flight with the Mercury and X-15 flight programs in the early 1960's.

In the 1960's, several programs successfully generated aerothermodynamic flight data to improve the understanding and interpretation of theoretical and ground test results. The ASSET and PRIME programs flown in the early and mid-1960's provided aerothermodynamic flight data for ablative and metallic thermal protections system (TPS) concepts. The Apollo 4, FIRE I, and FIRE II programs^{2,3} provided flight data to validate predictions from theoretical radiation models and arc-jet ground test results in support of the return from lunar and planetary missions. The single flight Reentry F vehicle⁴ was also flown in the 1960's and returned the benchmark data still used today for hypersonic boundary-layer transition predictions at Mach numbers up to 20 and altitudes down to 60,000 ft.

The X-15 research program⁵⁻⁸ was flown throughout the 1960's at Mach numbers to 6.7 and altitudes to 354,000 ft. The Sandia Winged Energetic Reentry Vehicle Experiment (SWERVE) vehicles⁹ have provided

much of the aerothermodynamic data obtained during the 1970's and 1980's. Currently the Space Shuttle^{10,11} and the Pegasus® vehicle¹² are providing aerothermodynamic flight data for correlation with ground test results.

Flight experiments are viewed by much of the community as the final validation of the ground test. This provided much of the impetus in designing, building, and flying a number of the hypersonic vehicles listed here. For example, the renowned scientist Hugh L. Dryden stated at the 1956 X-15 Conference,¹³ "The X-15 project is proceeding on an expedited basis with the intention of realizing flights of a man-carrying aircraft at hypersonic speeds as soon as possible for *exploration to separate the real from the imagined problems and to make known the overlooked and the unexpected problems*" (emphasis added by the the authors). No better description of a research program could be stated.

Facility capabilities growth has occurred because the flight test programs are focusing attention on the simulation and ground test facilities. In addition, new facilities may be developed as the experimenters are challenged by the flight data. These challenges may come from unexpected phenomena or from unexpected differences between the predictions and the flight results.

One important reason for the intense focusing seen in the X-15 and Space Shuttle programs was their crewed status; staking a person's life on the correctness of predictions requires a bigger effort and more conservatism than does flying an uncrewed vehicle.

The value of flight experiments will be demonstrated in the discussion in this paper of the X-15, the Reentry F, the SWERVE, and the Space Shuttle. This paper discusses aerodynamic and aerothermodynamic issues from which a variety of lessons were learned for these vehicles, with comparisons between flight and ground test results. A more thorough discussion of the value of flight experimentation may be found in Ref. 10.

Data Presentation

In fields as diverse as aerodynamics and aerothermodynamics, comparisons between flight and ground results inevitably cover a wide variety of phenomena and their accompanying nomenclature. This paper is a summary of the more conspicuous cases and is limited in length and depth. As a result, the data comparisons between ground test and flight test are usually taken exactly as they appeared in the original referenced

document. Unfortunately, full interpretations of the results may not be evident to the nonspecialist, so it is left to the reader to go to the original referenced documents for more complete treatment of the phenomena. Statements from these documents are frequently taken nearly verbatim to ensure that they are consistent with the discussion of the figures. The intent here is only to expose the reader to the variety of meaningful aerodynamic and aerothermodynamic ground and flight test results to show the way flight data (sometimes incidental) can be used to bring to light entirely new phenomena.

X-15 Experience

The primary purpose of the X-15 program was to focus the research required to support manned hypersonic flight within and outside the earth's atmosphere and to develop a flight research program to assess the various problem areas associated with hypersonic flight. The specific X-15 performance requirements were:

1. to achieve 6,600 ft/sec maximum velocity,
2. to be capable of flying to at least 250,000 ft,
3. to have representative areas of the primary structure experience temperatures of 1200 °F, and
4. to have some portions of these representative structures achieve heating rates of 30 BTU/ft²/sec.

The X-15 met or exceeded the first three of these requirements. The fourth requirement was only met where shock impingement caused extremely high heating rates, as discussed in a following section. Some significant aerothermodynamic results are summarized in the following sections. A photograph of the X-15 aircraft is shown in Fig. 1 and a cutaway drawing in Fig. 2.

One primary research area was to investigate aerodynamic heating at hypersonic speeds. A considerable amount of heating data were obtained¹⁴⁻¹⁹ and a number of problem areas were uncovered. These problems included premature boundary-layer transition, correlation of measured and calculated turbulent heat transfer, windshield damage, flight-wind tunnel heat transfer correlation, shock impingement heating, and interference heating.

Boundary-Layer Transition

The condition of the boundary-layer flow over a surface, whether laminar or turbulent, has a great impact on the total heating load and maximum temperatures at specific locations on a vehicle. Although

®Pegasus is a registered trademark of Orbital Sciences Corp., Fairfax, VA. The Pegasus vehicle was developed as a private joint venture between Orbital Science Corp. and Hercules Aerospace Corp., Magna, UT.

the X-15 design criteria used a conservative approach to boundary-layer transition, the boundary layer still transitioned to turbulent flow well upstream of where this had been anticipated. For the wing of the X-15, this premature transition was caused by the stream-wise expansion slots that were designed into the leading edge to allow for thermal expansion.¹⁴ With the exception of these slots, the leading edge of the X-15 was a solid bar of Inconel X[®] which served as a heat sink. The boundary-layer transition is shown in Fig. 3.

Two methods were used to detect laminar and turbulent areas. The first was the thermocouple data reduced to heat-transfer coefficients. The second was the use of temperature sensitive paints. The upper right of Fig. 3 shows a contrast enhanced post-flight photograph of the lower surface of the X-15 wing. The line dissecting the wing image shows location of the mid-semispan thermocouple row. The post-flight temperature sensitive paint patterns show the wedge shaped areas of turbulent flow emanating from the leading-edge expansion slots. Also shown in Fig. 3 is a comparison of the measured and calculated values for normal transition and for cases where the boundary layer is tripped by the previously mentioned thermal expansion slots at the leading edge. As shown, the heat transfer coefficients for the turbulent flow are more than double the laminar flow values. To alleviate this problem, shields were used to cover the leading-edge slots (Fig. 4). However, even with the leading-edge slots covered, most of the X-15 wing surface experienced turbulent flow. The lip or ridge behind the ball nose is believed to have tripped the boundary layer on the fuselage. Consequently, most of the wetted surface of the X-15 airplane experienced turbulent flow during its flights at hypersonic speeds.

Correlation of Measured and Calculated Turbulent Heat Transfer

A primary objective of the X-15 research program was to measure turbulent heat transfer coefficients and to compare the results to various prediction methods. Comparisons between measured and calculated values were reported in Refs. 14 through 17. The results from these reports indicated that the effect of wall-to-recovery temperature on the turbulent heat transfer coefficient was less than that predicted by theory and that good agreement between measured data and calculated values was obtained if the effect of wall-to-recovery temperature ratio was neglected. Consequently, during the early 1960's wall-to-recovery temperature ratio was neglected when calculating X-15 surface temperature. Results from Ref. 20 show that this procedure

produced good agreement between measured and calculated X-15 temperatures.

It was recognized at the time that these results might be fortuitous, since there were unknown internal conduction and radiation losses and that the boundary-layer edge flow conditions were not accurately known. It was, therefore, considered that these factors could be causing the discrepancies between the theoretical, predicted values and the measured data. Consequently, an experiment was devised and flown on the X-15 that sufficiently reduced these unknown factors.²¹ Heat transfer coefficients were obtained at wall-to-recovery temperature ratios of 0.22 to 0.33 at a Mach number of 5.25. The results showed that when the heating losses were sufficiently reduced and the boundary-layer edge flow condition accurately known, the effect of wall-to-recovery temperature ratio predicted by the theories was correct and the agreement between flight measured and theoretical turbulent heat transfer was good.

Windshield Heating

The windshield glass originally installed on the X-15 was soda-lime tempered plate glass.²² This choice was based on a predicted maximum temperature of 750 °F. Data from early flights indicated that the temperature would be near 1000 °F and that the differential temperature between the inside and outside surfaces of the windshield would be 750 °F. It was apparent that the soda-lime glass would not withstand these temperatures and temperature gradients. Therefore alumino-silicate glass was installed in all three X-15 airplanes; however, one of the soda-lime windshields was inadvertently reinstalled at a later date. It fractured during recovery from a high-altitude flight of 217,000 ft, as shown in Fig. 5. In addition, on a flight to Mach 6.04, one of the alumino-silicate glass panels fractured, as can be seen in Fig. 6. Both failures were caused by buckling of the glass retainer frame due to thermal stresses resulting from high temperature gradients. The problem was solved by changing the retainer from 0.05-in. thick Inconel X to 0.10-in. thick titanium.

Flight-Wind Tunnel Heating Correlation

When the X-15 airplane was being built the ability to predict the level of turbulent aerodynamic heating at hypersonic speeds was limited. Therefore, wind tunnel measurements of aerodynamic heating were made on a 0.0667-scale model of the X-15.²³ Subsequent flight measurements¹⁸ showed that for some locations on the airplane the wind tunnel data were in poor agreement with the flight heat transfer measurements. Figure 7 illustrates the discrepancy between X-15 flight and wind tunnel heating data. This figure shows the correlation of flight and wind tunnel data for the lower fuselage centerline. The low angle of attack wind tunnel data (α between 0 and 2°) are 50 to 100 percent higher

[®]Inconel is a registered trademark of International Nickel Company, Huntington, WV.

than the flight data. This discrepancy was the result of roughness effects caused by the transition strip that was required for the wind tunnel model to assure turbulent flow. The wind tunnel data at high angle of attack (α of 15 to 16°) are much higher (300 percent) than the flight data, and these large differences are due to roughness effects caused by the transition strip on the wind tunnel model and to a significant variation in the total temperatures along the wind tunnel vertical centerline.¹⁸

Shock Impingement and Interference Heating

The following discussion of the shock impingement and interference heating experiences on the X-15 is taken from Ref. 24.

Shock Impingement

The first experience with severe structural damage on a hypersonic aircraft due to a combination of shock impingement and interference effects on local heat transfer occurred on a performance envelope expansion flight of the X-15-2 research airplane. The heating damage was near a dummy hypersonic ramjet engine mounted on a pylon (unswept modification of the ventral fin) at the rear end of the fuselage. The flight, planned to test an ablative coating and evaluate the handling qualities of the airplane with the dummy ramjet installed, reached a maximum Mach number of 6.7 at an altitude of 99,000 ft.

It was known that when shock impingement occurs near the reattachment point of a separated flow region or near the origin of an attached boundary layer, the local heating is from five to ten times the undisturbed level. When there is no flow separation and the shock impingement occurs after the attached leading-edge flow is well developed, the increase in heating is in direct relation to the increase in pressure and could be predicted by the appropriate choice of either laminar or turbulent infinite-cylinder boundary-layer theory.

The highest heating rates due to shock impingement occur when the leading edge is unswept. Sweeping the leading edge tends to relieve flow separation and the related extreme heating conditions that result from combining shock impingement and flow reattachment. However, even with highly swept leading edges, the heating rate can be four to six times the undisturbed laminar level because of the increase in pressure and the boundary-layer transition to turbulent flow caused by the impinging shock.

Figure 8 is a pre-flight photograph of the dummy ramjet engine pylon. The entire pylon and most of the dummy ramjet engine were coated with ablative material for thermal protection. Post-flight photographs (Figs. 9(a) and 9(b)) show the melting damage on the

pylon caused by the shock impingement heating. The interference heating area is also indicated in Fig. 9(a). The shock pattern in the X-15 ramjet-pylon area is extremely complex. A postulated shock pattern is shown in Fig. 10. The shocks generated by the ramjet spike tip, spike flare, cowl lip, and bottom impact pressure probe interact near the ramjet-pylon junction. It appears from post-flight inspection that the four lower impact pressure probes failed at the root because of very high temperatures and resultant loss of strength or melting at the root.

The most severe melting damage was on the leading edge near the bottom impact pressure probe. To determine the temperature in this area, the calculated undisturbed heat transfer coefficient was increased by a factor to match the measured substrate temperature data. The factor was applied to infinite-cylinder laminar boundary-layer theory assuming an ablator leading-edge radius of 0.825 in. and freestream conditions ahead of the leading edge to obtain the cold-wall heat flux time history for the flight. This calculated heat input was then used in the NASA Langley Research Center charring ablator computer program to compute the substrate temperature up to the time in the flight when the ablator in the impingement zone was consumed. Because of expected scouring action in the shock impingement zone, the assumption was made that the charred ablator was removed immediately as it was formed so that the virgin ablator was constantly exposed to the stream. The actual leading-edge radius in the shock impingement zone at any time during the first part of the flight was not known, and it was assumed to remain constant at the initial value of 0.825 in. until the ablator burned through. By using the calculated substrate temperature at the time of ablator burn through in the shock impingement zone as the initial temperature, the temperature time history of the exposed leading edge with a 0.375-in. radius was then calculated for the remainder of the flight. The calculated temperature time history of the leading edge in the shock impingement zone is compared with the measured leading-edge temperature in Fig. 11.

The primary objective in comparing the calculated temperature in the shock impingement zone with the nearest available measured temperature was to match the ablator burn through time (about 140 sec. from launch) by increasing the undisturbed pylon stagnation line heat-transfer coefficient by known factors. The match of the ablator burn through time as shown in Fig. 11 was obtained with a factor of 9. The difference of the slopes of the measured and the calculated data after burn through can be attributed to the location of the thermocouple outside the shock impingement zone. The figure shows that the calculated leading-

edge temperature increased rapidly to near-equilibrium temperature after ablator burn through.

Interference Heating

The ablator was completely eroded away on the bottom of the fuselage around the pylon root leading edge. The bare fuselage skin can be seen in Fig. 9. Some permanent skin deformation resulted.

The configuration of the fuselage and the pylon leading edge is similar to a flat plate with an attached cylinder of zero sweep. A factor of 7 times the turbulent flat-plate heat-transfer coefficient using the flow length of 40.45 ft was used in an attempt to calculate the substrate temperature time history. The calculated cold-wall heat-flux time history was used as an input to the charring-ablator computer program to determine the substrate temperature and the probable time at which the ablator was completely removed, assuming immediate char removal. When the ablator was removed, the skin temperature time history was continued through the remainder of the flight by using a "thin-skin" calculation. Since no data were obtained at this location, the calculated temperature shown in Fig. 12 represents the best estimate of what occurred in flight. It appears that the calculated heat-transfer coefficient, increased by a factor of 7, resulted in a substrate temperature that corresponded favorably with the observed condition of the structure. The 1400 °F temperature would have been sufficient to cause the observed permanent skin buckling in the fuselage interference zone, but the temperature was far below the melting point of Inconel X.

The X-15-2 experience emphasizes the need for extreme care in the design of hypersonic vehicles to eliminate or minimize shock impingement and interference heating effects. For the stagnation case with shock impingement, temperatures may even exceed the limits of such high-performance metals as columbium (melting point 4400 °F) and tantalum (melting point 5300 °F).

Recapitulation of Aerothermodynamic Results

The X-15 flight program experience provided new insights into many important areas that affected that program and subsequent programs. Several of the many results are discussed here. To emphasize the key results from the previous discussion, the following is a recapitulation of the aerothermodynamic results.

The boundary layer transitioned to turbulent flow well upstream of where transition was predicted by the wind tunnels because the wind tunnels were unable to duplicate the Reynolds number and surface irregularities of the X-15. Nearly all of the surface of the X-15 experienced turbulent flow hypersonically.

Good agreement was found between flight measured and theoretical turbulent heat transfer, if the boundary-layer edge flow conditions were accurately known and the heating losses were accounted for.

The increase in the maximum temperature (from the predicted maximum 750 °F to the flight measured 1000 °F) caused the thermal stresses resulting from the higher temperature gradients to buckle the windshield glass retainer frame. This failure required a redesign of the windshield glass retainer.

The hypersonic turbulent aerodynamic heating measured in flight was considerably lower than the wind tunnel predictions at high and low angles of attack, caused in part by the roughness of the wind tunnel transition strip.

The data showed that local heating rates caused by unexpected shock impingement were 9 times that of the undisturbed level. This correlated well with predictions from prior general studies.

The vehicle also demonstrated that the local heating rate caused by unexpected interference heating was 7 times the turbulent flat plate heat-transfer coefficient, which was in good agreement with predicted flat plate heating rates near a junction of a plate and a cylinder.

Reentry F Experience

The Reentry F vehicle was a single vehicle flown only one time. The data from this flight have been used to benchmark theory and ground test data for the past 20 years. The following information is extracted from Ref. 4.

A 13-ft conical body, with a half-angle of 5° and an initial nose radius of 0.10 in. was flown to extend turbulent heat-transfer data to conditions of high local Reynolds number and Mach number.⁴ The Reentry F flight test also provided experimental data on boundary-layer transition during reentry. This section presents the experimental results obtained for the beginning and end of boundary-layer transition during reentry from an altitude of approximately 100,000 to 60,000 ft at a freestream Mach number of 20.

The prime experimental data obtained during reentry consisted of temperature measurements of the beryllium wall at 21 locations (Fig. 13) on the spacecraft. There were 12 measurement stations along the primary ray ($\phi = 0^\circ$) and 5 stations along the opposite secondary ray ($\phi = 180^\circ$). In addition, thermal sensors were located at the 90° and 270° circumferential positions at the 73.0- and 144.0-in. stations.

The flight profile of the reentry is shown in Fig. 14, with freestream Mach number plotted against altitude and time. The data period is also shown on this figure.

The flight measurement data were assessed and corrected with respect to various uncertainties such as local flow conditions as described in Ref. 4, but the corrections do not directly affect the data presented in this paper.

Boundary-Layer Transition Data

Heating rates at each thermal measurement station were computed from the smoothed measured temperature histories by the method of Ref. 25. The beginning and the end of transition are defined here as the intersections of the curves faired through the laminar, transitional, and turbulent heating data, as shown by these heating rate distributions in Fig. 15. The transition locations presented are accurate to within ± 0.5 ft.

Beginning of Transition

The initial movement of transition onto the spacecraft occurs at an altitude slightly above 100,000 ft. Heating rate distributions along the primary ray are presented in Fig. 16. The heating rate distributions at altitudes of 96,000, 87,000, 80,000, and 74,000 ft are presented, with the beginning of transition as determined from heating rate distribution noted at each altitude. Figure 17 shows the axial locations of the beginning of boundary-layer transition, as determined from the heating rate distributions at 2000-ft intervals for altitudes from 100,000 to 60,000 ft. This figure illustrates the forward motion of the beginning of boundary-layer transition with decreasing altitude.

End of Transition

The forward motion of the turbulent front (end of transition) is also shown in Fig. 17. The turbulent front lagged the beginning of transition by approximately 4 ft to an altitude of approximately 66,000 ft. Below this altitude, the turbulent front appeared to remain stationary at the 7.5-ft station.

It was concluded that the Reynolds number change over the transition region correlated with the transition Reynolds number for experimental cone data from flight and ground test.⁴ It was also noted that the trends in the effects of nose blunting that occurred on the Reentry F flight were similar to the effects previously seen in wind tunnels.

Effect of Angle of Attack on Transition on Reentry F

The symmetry of boundary-layer transition is influenced by the angle of attack of the test vehicle. The Reentry F was flown at a small, nonzero angle of attack. The primary ray was on the leeward side and the secondary ray was on the windward side.

Figure 18 shows the end of transition on each of the four axial rays, where $\phi = 0^\circ$ was the primary ray and $\phi = 180^\circ$ was the secondary ray. It is obvious from this figure that the end of transition is not symmetrical about the body. For these data, transition on the windward side (secondary ray) is observed to be consistently farther forward than on the leeward side (primary ray).

This result was contrary to most of the current wind tunnel transition data at angle of attack, which showed that transition moved farther forward on the leeward side. However, the effect shown with Reentry F had been observed on a few wind tunnel tests.

SWERVE Flight Test Experience

Sandia designed, developed, and conducted three flight tests of a slender hypersonic vehicle called SWERVE.⁹ The first flight test occurred in 1979 and the last in 1985. All vehicles flown were spherically blunted conical vehicles. The cone half-angle in all cases was 5.25° and the third vehicle was a little over 100-in. long. The nose tip radius to base radius ratio was about 0.07. Small wings and elevons were used to increase lift and provide control. The heat shield and nose tip were ablative materials. The vehicle was flown out of the Kauai Test Facility and, in the case of the third flight, reentered near Johnston Island. Extensive wind tunnel testing produced a large database on this shape. Figure 19 shows the extent of the database for the Reynolds number based on vehicle length as a function of Mach number. Some of the flight test experience from this flight, relating to aerodynamics and aerothermodynamics, is summarized in the following paragraphs. A complete simulation of aerodynamics, aerothermodynamics, dynamics, trajectories, and autopilot were done pre-flight.

The SWERVE maneuver from the third flight (Fig. 20) included a -10° -angle of attack, Mach 12, high-altitude pull out at 20 sec, requiring control deflections of 4° , followed by a return to 0° -angle of attack at 60 sec at about Mach 8. Pre-flight it was assumed the boundary layer would be laminar at Mach 14 and turbulent at Mach 8, so the boundary layer was artificially tripped in the Mach 8 wind tunnel studies to ensure a turbulent boundary layer. The responses predicted by the wind tunnel at Mach 14 and 8 are compared to the flight data in Figs. 21 and 22 respectively. The Mach 14 wind tunnel data accurately predicted the control deflection observed in flight at Mach 8 and the Mach 8 wind tunnel data matched the control deflection from flight at Mach 12. Surprisingly, the flight data exhibited a turbulent boundary layer at Mach 12 and a laminar boundary layer at Mach 8, which accounted for some of the peculiar agreement between the flight and wind tunnel predictions. In addition, there was

disagreement pre-flight as to which wind tunnel and limited computational fluid dynamics (CFD) predictions would more accurately predict the flight results. Recently, a parabolized Navier-Stokes (PNS) code has been used to predict the control surface deflection (δ). This PNS code accurately matched the Mach 14 laminar and Mach 8 turbulent wind tunnel data. The PNS code predictions, which used values that matched the boundary-layer states observed in flight, are shown in Tables 1 and 2 (Mach 12 turbulent and Mach 8 laminar). The PNS results accurately predicted the control deflection for Mach 12 (turbulent) but were not as close for Mach 8 (laminar); 20-30 percent difference still exists. The PNS prediction, which is a function of the Reynolds number and boundary-layer state, is still incorrect in some places. The wind tunnel prediction and CFD results still do not agree well with flight in some areas.

Table 1. PNS results for Mach 12 with turbulent boundary layer.

Parabolized Navier-Stokes results (Mach 12)				
α , deg	δ , deg	C_N	X_{CP}/LB	C_m
10	0	0.476	0.701	-0.00529
10	5	0.452	0.687	0.00114
10	10	0.437	0.6878	0.00514
$M = 12$		$\delta_{TRIM} = 4.11^\circ$		
Turbulent		$T_W = 4000^\circ R$		

Table 2. PNS results for Mach 8 with laminar boundary layer.

Parabolized Navier-Stokes results (Mach 8)				
α , deg	δ , deg	C_N	X_{CP}/LB	C_m
2	0	0.0930	0.721	-0.00291
2	2	0.0861	0.702	-0.00107
2	5	0.0756	0.667	0.00175
$M = 8$		$\delta_{TRIM} = 3.1^\circ$		
Laminar		$T_W = 2000^\circ R$		

Boundary-layer transition was determined post flight from thermocouple and photodiode data. Flight measured temperatures at about the midpoint of the cone are shown in Fig. 23, with pre-flight predictions with the General Electric low mass addition (GELMA) criteria and with CFD results assuming the entire flight is laminar. The oscillation at the end of the time history was caused by changes in the angle of sideslip. Figure 24 shows photodiode data on opposite sides of the cone at the 89-in. station which indicates that when the attitude of the vehicle was changed the windward-side flow (180° ray) went from laminar to turbulent (full-scale or 100 unit photodiode indication) and the

leeward-side flow (0° ray) went from turbulent to laminar. Using the boundary-layer state observed in flight (such as that for the photodiode data shown in Fig. 24) resulted in the flight-corrected CFD curve shown in Fig. 23, which matches the flight data very well. There were over 100 thermocouples installed throughout the vehicle thermal protection system (TPS) and agreement between flight and prediction was very good once the boundary-layer state pattern observed in flight was used in conjunction with the prediction. Figure 25 shows the GELMA criteria and the state of the boundary layer observed in flight. The criteria clearly are not adequate for this flight.

In summary, the SWERVE vehicle has been flight tested three times. The data discussed in this paper are from the third flight. A large wind tunnel database exists with sophisticated CFD codes to predict flight conditions. Some uncertainty still exists in the aerodynamic database and large uncertainty exists in the prediction of boundary-layer state, as shown in the differences between the predicted values and the flight values. The boundary-layer state affects the aerodynamic state and has a major impact on the aerothermodynamics, affecting the adequacy of the TPS.

Space Shuttle Experience

Since 1981 the Space Shuttle (Fig. 26) has provided many opportunities to compare ground test to flight test for aerothermodynamic data. Many of these comparisons are discussed in the literature. This section summarizes some of the more significant results published to date. The comparison is primarily from the ground test perspective.

The flight data that have been used were from the available Space Shuttle instrumentation. A complete description of this instrumentation is given in Ref. 26. This reference discusses the specific orbiter experiments (OEX) that were performed to enhance the understanding of the aerothermodynamic phenomena as well as the orbiter operational instrumentation (OI) that is taken on all of the Space Shuttle flights.

The Space Shuttle orbiter is a large double-delta-winged vehicle designed to orbit the Earth, enter the atmosphere, and land horizontally. A number of topics in Space Shuttle hypersonic experience are discussed in Ref. 10. Some of this discussion is repeated in the following.

In this section, after the RCS jet interaction is examined, heating will be discussed in three sections: windward, OMS pod, and leading edge. The topic is discussed this way because different physical phenomena influence the heating in these areas.

RCS Jet Interaction

The Space Shuttle trajectory during reentry, and, therefore, its heating profile, are controlled through a series of energy management bank reversals. The vehicle is controlled by conventional aerodynamic surfaces and by the reaction control system (RCS) jets. The first bank reversal on the first Space Shuttle flight, STS-1, resulted in a significantly larger response than predicted.²⁷ This flight maneuver, at Mach 24, is compared to the predicted maneuver in Fig. 27. The flight maneuver resulted in angle of sideslip peaks twice the size of those predicted and in somewhat higher roll rates than predicted. Angle of sideslip excursions this large move an area of high heating off the reinforced carbon-carbon (RCC) nosecap. The motion is also much more poorly damped than predicted. Comparing the predicted maneuver with the actual maneuver it is obvious that the flight stability and control derivatives were significantly different from the predictions. These stability and control flight maneuvers were analyzed with the maximum likelihood method and the resulting flight determined estimates were used to modify the flight simulator significantly.

Simulation studies resulted in modifying the control inputs for the bank reversal maneuver on STS-2, as shown in Fig. 28. Nearly identical maneuvers were flown on all subsequent Space Shuttle flights. The primary problem with this and other high-altitude maneuvers was obvious from the flight-determined rolling moment due to yaw jet (L_{YJ}). Figure 29 (from Ref. 28) shows flight-determined and predicted L_{YJ} as a function of Mach number. The predicted variations are also evident on this figure. These variations represent the uncertainty in the predictions, as determined by aerodynamicists and based on previous correlations between wind tunnel and flight-determined derivatives for similar aircraft.²⁹ At the highest Mach numbers the value of the flight-determined L_{YJ} was outside these variations.

To understand the difference between flight and prediction it is necessary to briefly describe how the predictions were made. More complete descriptions are given in Refs. 30 and 31. The forces and moments are broken down into three components; pure thrust, jet impingement on the Space Shuttle body, and jet interaction with the flow around the Space Shuttle. The jet interaction term is the one of interest here and the remainder of this discussion will concentrate on jet interaction effects. The wind tunnel tests were conducted for Mach numbers between 2.5 and 10. Since the wind tunnel tests were limited to Mach numbers below 10 and dynamic pressures above 75 ft²/lb, the predictions for higher altitudes and higher Mach numbers were obtained by varying momentum ratio and mass-flow ratio

to include those values applicable for the higher altitudes. Figure 30 shows the comparison of the flight-determined and predicted jet-interaction terms. This figure shows that the flight rolling moment due to RCS jet interaction (determined with maximum likelihood estimation) was smaller than predicted, particularly above Mach 15 at an altitude greater than 200,000 ft. The explanation for this high-altitude jet simulation error lies in the description of the flow field surrounding the side jet exhaust.³⁰ At high altitudes, the vehicle angle of attack is approximately 40°, which causes flow separation on the upper surface of the wing. When the RCS side jets are fired, the exhaust enters this separated flow region and pressurizes the volume defined by the wing upper surfaces and the flow separation wake boundaries.

The aerodynamic flow field for this high-altitude flight environment cannot be properly simulated in the wind tunnel. For example, at the first bank maneuver (Fig. 27) at Mach 24, the flight dynamic pressure is 14 lb/ft². In these conditions, the wake boundary is much more easily deflected on the flight vehicle than on the wind tunnel model. This difference in high-altitude pressure levels strongly influences the differences observed between flight and predicted side-jet rolling moment jet interaction. The phenomena are described more completely in Ref. 30.

These results show the limitations of the wind tunnel database in predicting high-altitude jet effects. The vehicle wake flow parameters such as ambient pressure cannot be duplicated in the tunnel.³⁰ A limited amount of wing pressure flight data was studied and trends similar to those discussed previously for the maximum likelihood results were found.³¹ The flight-derived forces and moments due to up- and down-firing jets (used primarily for pitch and roll commands at low dynamic pressure) are discussed in Ref. 28. The correlation of these jet interaction terms was found to have the same limitations as those discussed for L_{YJ} .³⁰

Windward-Side Heating

There are two significant influences on windward heating. The first is the chemical state of the flow, either equilibrium or nonequilibrium. In nonequilibrium flow, surface catalysis becomes an important element in heating. The second influence is the state of the boundary layer, either laminar or turbulent.

Catalytic Effects

The design of the Space Shuttle orbiter TPS was based on predicted aerothermodynamic environments which were generated assuming that the orbiter flow field was everywhere in chemical equilibrium.³² Detailed pre-flight calculations indicated, however, that significant chemical nonequilibrium would persist over

the majority of that portion of orbiter entry when significant aerodynamic heat transfer occurs. The parameter which most significantly influences the level of surface heat transfer in such a flow field is the catalytic efficiency of the TPS surface with respect to the recombination of dissociated oxygen atoms. The catalytic efficiency of the reaction-cured glass (RCG) coating of the orbiter TPS tiles was thought to be relatively low, based on arc tunnel experiments. Therefore, flight heating rates were expected to be lower than "equilibrium chemistry" predictions as a result of the combination of nonequilibrium chemistry and a TPS surface which was not fully catalytic. Indeed, surface temperatures were found to be lower than the conservative predictions on the early flights.³³

In light of the great interest in noncatalytic surface effects, an experiment was conducted on STS-2 through 5 to study catalytic.³³ Thermal data for these especially modified tiles were collected on flights STS-2, -3, and -5. Selected centerline tiles, with previously installed instrumentation, were painted or overcoated with highly catalytic material. The purpose of the experiment was to demonstrate the noncatalytic nature of the baseline tiles by comparing them with the characteristics of the more catalytic modified tiles. The flight data showed that the surface temperatures of the catalytically-coated tiles, solid symbols, (shown normalized) were substantially greater than those of the baseline tiles (Fig. 31) and because of this, the surface catalytic efficiency of the baseline tiles is low.

An unexpected effect occurred during the entries that serendipitously provided further information into the catalytic-noncatalytic nature of orbiter windward-surface heat transfer.³⁴ This unplanned experiment manifested itself in significant instantaneous changes or jumps in measured TPS surface temperatures (Fig. 32) at affected locations. These jumps were apparently the result of anomalous deposits of metallic oxides on portions of the lower surface TPS, caused by oxidation of upstream acoustic sensor covers. This provided evidence of a sudden change in catalytic.

Comparing the levels of heat transfer between STS-2 and STS-3 for these locations showed approximately 18 percent greater heating rate level below about 238,000 ft on the later flight (Fig. 33). One factor in this was concluded to be a mission-to-mission progressive contamination of the TPS surface. This conclusion was bolstered by the good correlation between the post-contamination data from STS-2 (round symbols) and the data from STS-3 (square symbols) before additional contamination occurred (Fig. 34).

As the flight program progressed, it became apparent that there was some change in the windward surface from flight to flight.³³ The surface temperature

was increased at the same flight condition, compared to previous flights. This led to the conclusion that the total emittance of the RCG coating decreased with the number of flights and surface catalytic efficiency of the coating increased (or surface temperature increased) with number of flights. The flight-to-flight changes in surface temperature can be seen in Fig. 31.

Surface contamination has been proposed as a possible cause of these changes. The general surface contamination comes from a variety of sources including impingement of burning solid rocket fuel and sea salt deposits while on the launch pad and local contamination comes, for example, from the oxidation, during entry, of upstream metal acoustic sensor covers.

When the aerothermal design of the Space Shuttle first started, heating predictions were heavily based on wind tunnel data, with modest computational modeling of catalytic.³² After the first five flights, heating predictions using computational models of the nonequilibrium chemistry were in use.³³ The thermal response predictions made with these models, including ground-test data, design trajectory, and reacting boundary-layer computation, agreed well in general with the flight data as is apparent in Fig. 35.

Nonequilibrium calculation techniques were used to predict heat fluxes to the windward side of the Space Shuttle orbiter.³⁵ The techniques were the axisymmetric viscous shock layer method, three-dimensional reacting Euler equations solutions coupled with axisymmetric analog boundary layer method, and a nonequilibrium three-dimensional viscous shock layer method. These calculation methods predicted heating trends but did not predict the measurements uniformly over the entire windward centerline for all flight conditions. That is, nonequilibrium methodologies could predict the heat flux for high-altitude reentry, but some improvements were still required. In particular, the key issue was determined to be the modeling of catalytic efficiency.

The models currently in use are capable of good agreement with the flight data³⁶ as is shown in Fig. 36.^{37,38} The addition of recent correlation for oxygen surface recombination gave better overall agreement with the flight data than the extrapolation of ground-based experimental recombination data. Predicted centerline and windward surface heat transfer were in good agreement with the flight data and the predicted trends in heating rates away from the windward symmetry plane appear correct. Future application of the current code for three-dimensional vehicle analyses appears promising based on such verification.

This progress in modeling is the result of obtaining flight data from which to infer the catalytic efficiency of the tiles and increases in computational capability

for model evaluation. This success in modeling the catalycity of Space Shuttle tiles using flight data indicates that obtaining flight data for other materials should result in good modeling of their catalycity.

In addition, the flight data also made it clear that the catalycity of a reusable vehicle should not be assumed to remain constant. Rather, it may be changed by the flight process. Contamination (the melted acoustic covers and the launch plume impingement), ground handling (the sea spray from the launch pad environment), and other factors all may change the properties of the surface.

Boundary-Layer Transition

Knowing the time and position of the boundary-layer transition is fundamental to determining the heating on the windward side of the Space Shuttle. Boundary-layer transition strongly contributes to the total heat load of the vehicle and the instantaneous heating rates. These two factors are important in determining the requirements of the vehicle's thermal protection.

A major element in boundary-layer transition is the roughness of the surface, such as the TPS tiles with which the windward surface is protected. To assess the effect of tiling patterns for these TPS tiles, a variety of grooves simulating tile gaps on flat plates were tested in the wind tunnel. It was determined that long grooves (or gaps) parallel to the streamlines produced more heating in the gaps. It was also discovered that grooves parallel to the surface streamlines produced strong boundary-layer tripping disturbances whereas grooves perpendicular to the streamlines produced much weaker interactions.³⁹ From these results the diagonal tiling pattern was established (Fig. 37).

In the original design the tiled surface was assumed to be smooth but in actual fabrication it became apparent that the surface would be much rougher than originally planned.⁴⁰ The tiles were paved with nominal gaps of 0.045 in. and have rounded edges. In addition, the edges of some tiles were irregular because of manufacturing techniques. Thus the surface was quite rough aerodynamically.³⁹ In fact, the lower surface, with its steps, gaps, and tile irregularities, is a complex surface in terms of roughness definition. Measurements were taken of a number of areas that appeared to be typically rough (Fig. 38) confirming this. The profilometer is able to resolve 0.001-in. surface displacements.

The original ground testing, assuming smoother tiles, was then repeated for the rougher actual tiles. This prompted the development of a more refined aerothermodynamic database with improved prediction technologies. These tests influenced the criteria for tile installation.

Wind tunnel tests were performed to examine boundary-layer transition using a 0.04-scale model with spherical roughnesses and simulated tiles. In the wind tunnel it was determined that the effects of the surface conditions dominated the upstream region and the effects of tunnel noise dominated the transition process in the downstream region. This suggests that transition predictions would be conservative in the downstream region and reasonably reliable in the upstream region.⁴⁰

It was originally predicted that transition would start at the aft end of the vehicle at about 900 sec and slowly move forward (Fig. 39). In flight, transition started much later than predicted and flashed to the nose almost instantaneously, as is also apparent in this figure. Figure 40 shows this more graphically with transition maps for the second flight.⁴¹ In this figure the transition contours for the left side of the Space Shuttle (the instrumented side) are mapped onto the Space Shuttle planform for three flight conditions. The transition front can be observed to flash forward instantaneously (i.e., between time = 76297 sec and time = 76298 sec) from the aft of the vehicle toward the nose. The complexity of the transition contours and the abrupt manner in which they moved, strongly indicate that the inflight transition process is dominated by the effects of discrete surface roughness.

The transition from laminar to turbulent flow at the aft end of the vehicle occurred later in the entry than expected, which also produced lower temperatures and a lower total heat load.⁴² Figure 41 shows the predicted and flight values of lower surface temperatures at the 70-percent location. The delay in transition can be clearly seen in the delayed increase in temperature.

It appeared, based on post-flight analysis, that the predictions could have been improved by removing the original, smooth-surface data from the correlation parameter as these data were very sensitive to freestream noise. However, even the rough-surface data seemed sensitive to tunnel noise.

The good agreement between the predicted and measured transition times in certain regions (such as the 10- to 20-percent centerline region) suggested that the simulations and correlation of transition in certain regions was very good.³⁹ The regions for which this was true had the transition process dominated by surface roughness and shock layer disturbances at wind tunnel and flight conditions, probably because of the relatively thin boundary layer and highly curved bow shock near the forward part of the orbiter. From this it was concluded that the wind tunnel data generated with effective roughnesses provided good predictions of flight conditions for the forebody. Differences between

predictions and flight values for the aft region were attributed to tunnel noise.

OMS Pod Heating

The OMS pod⁴³ has been investigated extensively because the heating of the pod is a critical factor in the ability of the orbiter to fly reduced angles of attack relative to development flight test and current operational levels. The position of the OMS pod (Fig. 26), extending from the orbiter side, makes it extremely susceptible to flow impingement (vortex scrubbing) and to damage from debris traversing along the fuselage. In all leeward side regions strongly influenced by vortex scrubbing, the wind tunnel data underpredicted the flight test data.⁴³ This is reflected in Fig. 42, showing predicted and flight temperatures for STS-2.

Vortex scrubbing is extremely sensitive to small variations in angle of attack, yaw, and Reynolds number. In flight it appeared that the flow becomes attached at a higher angle of attack and at a lower Reynolds number than under wind tunnel conditions. This sensitivity to angle of attack and flow attachment is particularly evident (Fig. 42) in the data collected in pushover-pullups (POPUs), which are characterized by large variations in angle of attack. The change in temperature during the POPU at Mach 20 is obvious and it can also be seen that the methodology did not predict this sensitivity.⁴² The reason that the methodology did not predict this is because the wind tunnel predicted that the impingement of the vortex flow would occur near 30°-angle of attack rather than at 37° as seen in flight.

Wing Leading-Edge Heating

There are two sources of heating of the wing leading edge; "boundary layer" heating and shock interaction.⁴⁴ In this section, the term "boundary-layer" heating refers to the heating where there is no shock interaction. The leading-edge instrumentation was designed to measure the effects of both types of heating.

Instrumentation (radiometers) was installed (Fig. 43) at stations 40-percent semispan (the glove), at 55-percent semispan, 80-percent semispan, and 98.6-percent semispan (the wing tip), and data were collected during the first five flights. The 55-percent semispan is in the peak entry heating zone due to shock interaction (discussed in the following) and 80-percent semispan is in the maximum entry airload zone.

The maximum heat rate of the leading edge is shown in Fig. 44, with both predicted values and flight radiometer data, as well as estimated values from the radiometer data and the model.

Wing Boundary-Layer Heating

The wing leading edge of the Space Shuttle was aerothermodynamically modeled in a simplified form as a 45°-swept cylinder with regions of higher sweep at the glove and the wing tip. Wind tunnel data were used with this model to produce the predictions prior to flight. (This method did not model the shock interaction at the 55-percent semispan location.)

As can be seen in Fig. 45 the predicted temperature at the 80-percent semispan (panel 16) matched the flight data extremely well. The flight data (based on the radiometer data) were within 2 percent of the pre-flight prediction. This good match verified the usability of swept-cylinder methods outside the shock interaction zone.

The heat rates in the glove (represented by the 40-percent semispan) and the wing tip (the 98.6-percent semispan) were both substantially overpredicted. This, however, had been expected since the swept cylinder approach is known to be conservative in regions of high sweep.

The onset of boundary-layer transition that was assumed in the prediction would have caused more heating at the wing tip. However, the actual transition behavior was quite different from that predicted and this additional heating did not occur. Thus the existing wing tip analysis method was adequate for predicting flight heating and overpredicted with respect to the predicted heating due to transition.⁴⁴

Wing Shock Interaction

In addition to the boundary-layer heating, which heats the entire leading edge, bow-shock and leading-edge shock interaction heats the leading edge locally, as discussed in Ref. 44. Analysis of schlieren data, oil flow patterns, and heat transfer data from wind tunnel tests indicated that the bow and leading-edge shock impinged with a resulting third shock and with the vortex-jet impingement on the wing. The main effects of this disturbance were expected to be increased heating at 55-percent semispan on the leading edge, earlier transition on the outboard portions of the wing lower surface, and vortex scrubbing on the outboard wing upper surface.

This shock impingement is difficult to scale from the wind tunnel to flight and both "following-shock" and "double-shock" techniques were used to scale wind tunnel data to predicted flight conditions.⁴⁴ As mentioned previously, instrumentation was installed at panel 9, at 55-percent semispan, to measure the heating caused by the shock interaction.

As can be seen in Fig. 46 the predicted temperature was 200 °F lower than that measured in flight during the period of peak heating. This is confirmed by comparing the solid and dashed lines showing the temperature distribution in Fig. 47.

It was found on subsequent flights that the temperature in this region was consistently about 200 °F higher than the predicted values. This difference confirms the difficulty of scaling wing shock interaction from the wind tunnel to flight.

Concluding Remarks

The preceding sections have shown how the correlation and validation of ground test and flight are used in a complimentary fashion to improve the results of each. The flight data provide benchmark data to improve interpretation and corrections to ground test results. These improved ground test techniques, coupled with other flight test data, allow improved vehicles to be designed, built, and analyzed with reduced technical risk.

Many examples given in the preceding sections show that the predictions from ground-based data were conservative. This is to be expected as uncertainty should result in conservative predictions. The objective is to design the flight vehicle with adequate margins to reduce the risk to the vehicle. At the same time it is also important to keep these margins low enough that the flight vehicle is versatile so, usually, its useful flight envelope can be expanded during flight test. Of course, much is learned in the validation of ground test with flight data even if the prediction is in complete agreement with flight. This agreement further reduces the margins that are required for future flight vehicles. In some cases, however, even the conservative ground test predictions are exceeded. When this happens much more is learned (assuming that the vehicle survives) as we may become aware of unknown phenomena or of the increased importance of known phenomena.

In the X-15 example previously discussed, the following unexpected results occurred. These are: the boundary layer transitioned upstream of prediction hypersonically, the increased thermal stress due to higher than predicted temperature on the windshield frame resulted in buckling, the hypersonic turbulent aerodynamic heating was considerably lower than predicted, and the shock impingement and interference heating resulted in considerable damage to the vehicle and were 9 and 7 times the undisturbed levels, respectively, as had been observed in generic wind tunnel tests.

The Reentry F vehicle flight data showed the same general aerothermodynamic characteristics as were obtained from the then-current wind tunnel predictions. However, the flight data showed that the end of

boundary-layer transition occurred farther forward on the windward side than on the leeward side. This disagreed with the results of most of the wind tunnel studies done at the time.

The Sandia Winged Energetic Reentry Vehicle Experiment (SWERVE) flight data unexpectedly showed that the flow was turbulent at Mach 12 and laminar at Mach 8. This resulted in disagreement between the predicted control deflections for the wind tunnel and computation fluid dynamic predictions. The flight data also, surprisingly, showed that during a change in attitude the windward side went from a laminar to a turbulent boundary-layer state and the leeward side went from a turbulent to a laminar boundary-layer state.

In the shuttle examples discussed here the vehicle exceeded the conservative predictions in three primary areas. These are: the RCS jet interaction with the flow over the vehicle, the angle of attack at which the vortex impinged on the OMS pod, and the wing leading-edge shock interaction heating.

References

- ¹Aerodynamic Design Data Book Orbiter Vehicle STS-1, Space Division, Rockwell International, SD72-5H-0060 Revision M, Nov. 1980.
- ²Ried, R.C., Jr., W.C. Rochelle, and J.D. Milhoan, *Radiative Heating to the Apollo Command Module: Engineering Prediction and Flight Measurement*, NASA TM-X-58091, 1972.
- ³Sutton, Kenneth, "Air Radiation Revisited," H.F. Nelson, ed., *Progress in Astronautics and Aeronautics: Thermal Design of Aeroassisted Orbital Transfer Vehicles*, Vol. 96, New York, 1985, pp. 419-441. (Also available as AIAA 84-1733.)
- ⁴Wright, Robert L. and Ernest W. Zoby, "Flight Boundary Layer Transition Measurements on a Slender Cone at Mach 20," AIAA 77-719, June 1977.
- ⁵Review of the X-15 Program. Weil, Joseph, compiler, NASA TN D-1278, June 1962.
- ⁶Becker, John V., "The X-15 Project," *Astronaut. & Aeronaut.*, Feb. 1964, pp. 52-61.
- ⁷Toll, Thomas A. and Jack Fischel, "The X-15 Project: Results and New Research," *Astronaut. & Aeronaut.*, Feb. 1964, pp. 20 et seq.
- ⁸Becker, John V., The X-15 Program in Retrospect, 3rd Eugen Sänger Memorial Lecture, Deutsch Gesellschaft für Luft und Raumfahrt, Dec. 1968.
- ⁹Williamson, W.E., Jr., "Hypersonic Flight Testing," AIAA 92-3989, July 1992.

¹⁰Iliff, Kenneth W. and Mary F. Shafer, "Space Shuttle Hypersonic Flight Research and the Comparison to Ground Test Results," (Invited), AIAA 92-3988, Aug. 1992.

¹¹*Shuttle Performance: Lessons Learned*, NASA CP-2283, 1983.

¹²Meyer, Robert R., Jr., Robert E. Curry, and Gerald D. Budd. "Aerodynamic Flight Research Using the Pegasus Air-Launched Space Booster," AIAA 92-3990, July 1992.

¹³Dryden, Hugh L., General Background of the X-15 Research-Airplane Project," In *Research-Airplane-Committee Report on Conference on the Progress of the X-15 Project*, pp. xvii-xix, 1956.

¹⁴Banner, Richard D., Albert E. Kuhl, and Robert D. Quinn, *Preliminary Results of Aerodynamic Heating Studies on the X-1 Airplane*, NASA TM-X-638, 1962.

¹⁵Quinn, Robert D. and Albert E. Kuhl, *Comparison of Flight-Measured and Calculated Turbulent Heat Transfer on the X-15 Airplane at Mach Numbers from 2.5 to 6.0 at Low Angles of Attack*, NASA TM-X-939, 1964.

¹⁶Banas, Ronald P., *Comparison of Measured and Calculated Turbulent Heat Transfer in a Uniform and Nonuniform Flow Field on the X-15 Upper Vertical Fin at Mach Numbers of 4.2 and 5.3*, NASA TM-X-1136, 1965.

¹⁷Quinn, Robert D. and Murray Palitz, *Comparison of Measured and Calculated Turbulent Heat Transfer on the X-15 Airplane at Angles of Attack up to 19.0°*, NASA TM-X-1291, 1964.

¹⁸Quinn, Robert D. and Frank V. Olinger, *Heat-Transfer Measurements Obtained on the X-15 Airplane Including Correlations with Wind-Tunnel Results*, NASA TM-X-1705, 1969.

¹⁹Banner, Richard D. and Albert E. Kuhl, *A Summary of X-15 Heat-Transfer and Skin-Friction Measurements*, NASA TM-X-1210, 1966.

²⁰Gord, P.R., *Measured and Calculated Structural Temperature Data from Two X-15 Airplane Flights with Extreme Aerodynamic Heating Conditions*, NASA TM-X-1358, 1967.

²¹Quinn, Robert D. and Frank V. Olinger, *Flight-Measured Heat Transfer and Skin Friction at a Mach Number of 5.25 and at Low Wall Temperatures*, NASA TM-X-1921, 1969.

²²Kordes, Eldon E., Robert D. Reed, and Alpha L. Dawdy, "Structural Heating Experiences of the X-15," In *Research-Airplane-Committee Report on Conference*

on the Progress of the X-15 Project: A Compilation of the Papers Presented, Nov. 1961, pp. 29-46. (Also available as NASA TM-X-711, 1962)

²³Price, Earl A., Nancy L. Taylor, and Paige B. Burbank, *Heat-Transfer Measurements of a 0.0667-Scale Model of the X-15 Airplane for an Angle-Of-Attack Range of 0° to 28° at Mach Numbers of 2.88 and 4.65*, NASA TM-X-821, 1963.

²⁴Watts, Joe D., *Flight Experience with Shock Impingement and Interference Heating on the X-15-2 Research Airplane*, NASA TM-X-1669, 1968.

²⁵Howard, Floyd G., *Single-Thermocouple Method for Determining Heat Flux to a Thermally Thick Wall*, NASA TN D-4737, 1968.

²⁶Throckmorton, David A., "Shuttle Entry Aerothermodynamic Flight Research: The Orbiter Experiments (OEX) Program," AIAA 92-3987, July 1992.

²⁷Iliff, Kenneth W., *Aircraft Parameter Estimation*, NASA TM-88281, 1987. (Also available as AIAA 87-0623, AIAA Dryden Research Lectureship Paper, Jan. 1987.)

²⁸Maine, R.E. and K.W. Iliff, "Selected Stability and Control Derivatives from the First Three Space Shuttle Entries," AIAA 82-1318, Aug. 1982.

²⁹Young, James C. and Jimmy M. Underwood, "The Development of Aerodynamic Uncertainties for the Space Shuttle Orbiter," *Shuttle Performance: Lessons Learned*, NASA CP-2283, 1983, pp. 1169-1185.

³⁰Stone, J.S., J.J. Baumbach, and B.B. Roberts. "Space Shuttle Orbiter Reaction Control Subsystem Flight Data Anomalies," *Shuttle Performance: Lessons Learned*, NASA CP-2283, 1983, pp. 381-395.

³¹Scallion, W.I., H.R. Compton, W.T. Suit, R.W. Powell, T.A. Blackstock, and B.L. Bates, "Space Shuttle Third Flight (STS-3) Entry RCS Analysis," AIAA 83-0116, Jan. 1983.

³²Ried, Robert C., "Orbiter Entry Aerothermodynamics," *Space Shuttle Technical Conference*, NASA CP-2342, 1983, pp. 1051-1061.

³³Stewart, David A., John V. Rakich, and Martin J. Lanfranco, "Catalytic Surface Effects on Space Shuttle Thermal Protection System During Earth Entry of Flights STS-2 Through STS-5," *Shuttle Performance: Lessons Learned*, NASA CP-2283, 1983, pp. 827-846.

³⁴Throckmorton, David A., E. Vincent Zoby, and H. Harris Hamilton II, "Orbiter Catalytic/Noncatalytic Heat Transfer as Evidenced by Heating to Contaminated Surfaces on STS-2 and STS-3," *Shuttle Performance: Lessons Learned*, NASA CP-2283, 1983, pp. 847-864.

³⁵Scott, Carl D., "A Review of Nonequilibrium Effects and Surface Catalysis on Shuttle Heating," *Shuttle Performance: Lessons Learned*, NASA CP-2283, 1983. pp. 865-889.

³⁶Thompson, R.A., "Comparison of Nonequilibrium Viscous-Shock-Layer Solutions with Shuttle Heating Measurement," *J. Thermophysics and Heat Transfer*, Vol. 4, No. 2, Apr. 1990, pp. 162-169.

³⁷Scott, C.D., "Catalytic Recombination of Oxygen and Nitrogen in High-Temperature Reusable Surface Insulation," *Progress in Astronautics and Aeronautics: Aerothermodynamics and Planetary Entry*, Vol. 77, 1981, pp. 192-212.

³⁸Zoby, E.V., R.N. Gupta, and A.L. Simmonds, "Temperature-Dependent Reaction Rate Expressions for Oxygen Recombination," H.F. Nelson, ed., *Progress in Astronautics and Aeronautics: Thermal Design of Aeroassisted Orbital Transfer Vehicles*, Vol. 96, New York, 1985, pp. 445-465.

³⁹Harthun, M.H., C.B. Blumer, and B.A. Miller., "Orbiter Windward Surface Entry Heating: Post-Orbital Flight Test Program Update," *Shuttle Performance: Lessons Learned*, NASA CP-2283, 1983, pp. 781-804.

⁴⁰Goodrich, Winston D., Stephen M. Derry, and John J. Bertin, "Shuttle Orbiter Boundary Layer Transition at Flight and Wind Tunnel Conditions," *Shuttle Performance: Lessons Learned*, NASA CP-2283, 1983, pp. 753-779.

⁴¹Hartung, L.C. and D.A. Throckmorton, "Computer Graphic Visualization of Orbiter Lower Surface Boundary-Layer Transition," *J. Spacecraft and Rockets*, Vol. 24, No. 2, Mar.-Apr. 1987, pp. 109-114.

⁴²Hertzler, Elam K. and Paul W. Phillips, "Flight Test Derived Heating Math Models for Critical Locations on the Orbiter During Reentry," *Shuttle Performance: Lessons Learned*, NASA CP-2283, 1983, pp. 703-718.

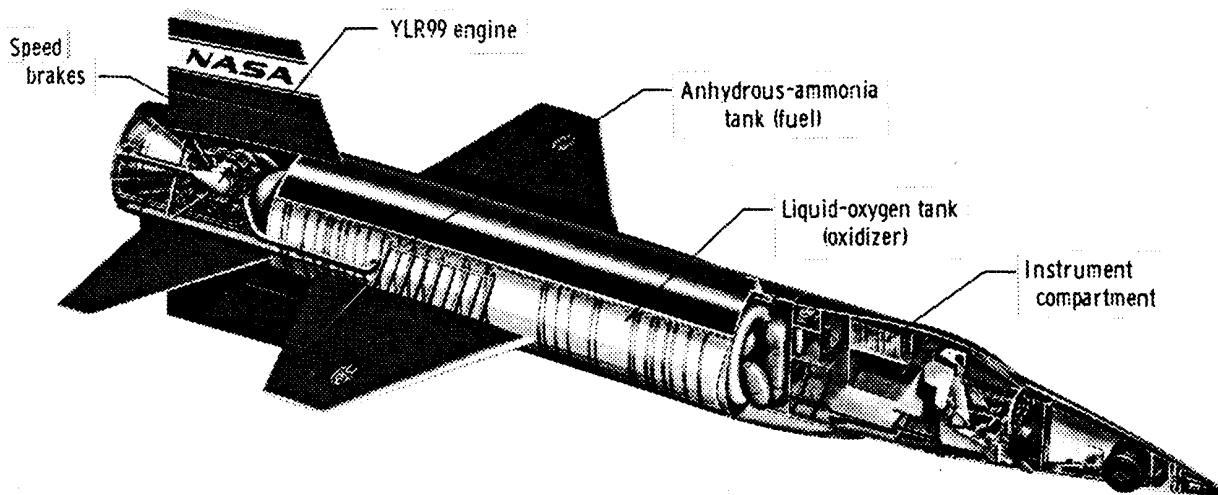
⁴³Haney, J.W. "Orbiter Entry Heating Lessons Learned from Development Flight Test Program," *Shuttle Performance: Lessons Learned*, NASA CP-2283, 1983, pp. 719-751.

⁴⁴Cunningham, John A. and Joseph W. Haney, Jr., "Space Shuttle Wing Leading Edge Heating Environment Prediction Derived from Development Flight Test," *Shuttle Performance: Lessons Learned*, NASA CP-2283, 1983, pp. 1083-1109.



E-7903

Fig. 1 The X-15 aircraft. (Ref. 18 Fig. 1).

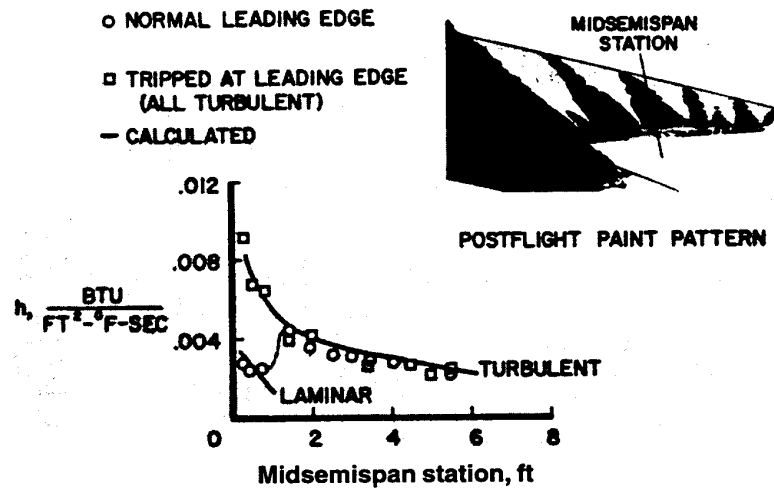


E-6990

Fig. 2 Cutaway drawing of the X-15 aircraft. (Ref. 18 Fig. 2).

WING BOUNDARY-LAYER TRANSITION

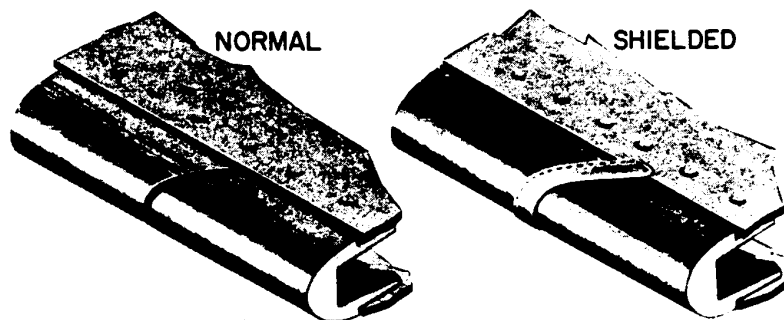
$M_\infty = 4, \alpha = 4^\circ$



920718

Fig. 3 Wing boundary-layer transition. (Ref. 14 Fig. 7).

WING LEADING-EDGE EXPANSION JOINTS



920719

Fig. 4 Wing leading-edge expansion joints. (Ref. 14 Fig. 8).

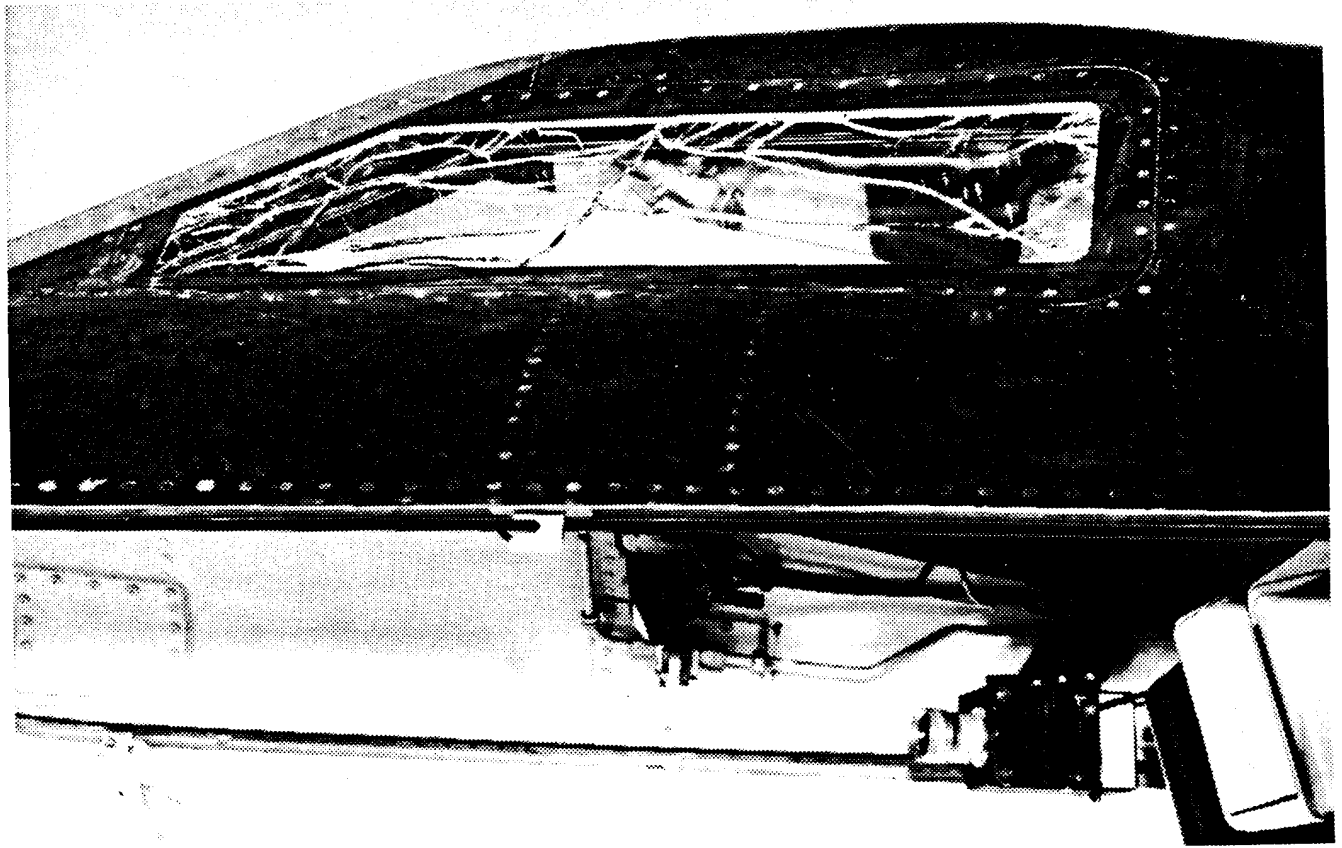


Fig. 5 Damaged windshield glass following flight to 217,000-ft altitude. (Ref. 22 Fig. 11).

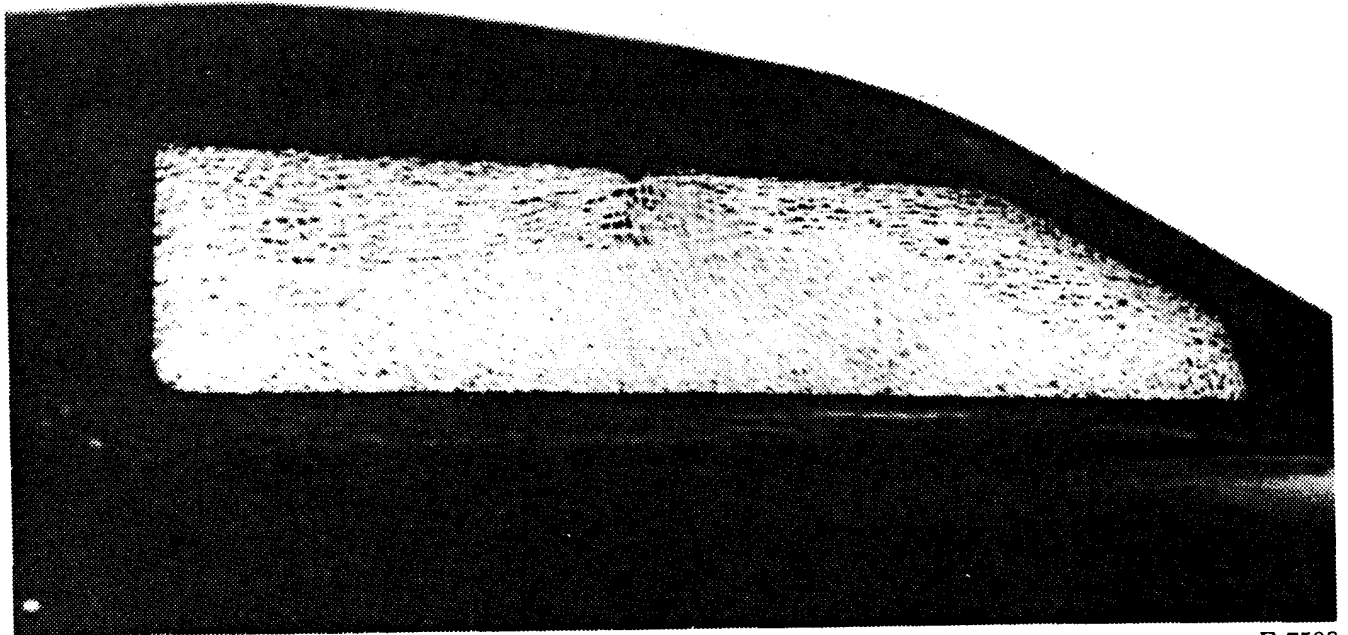
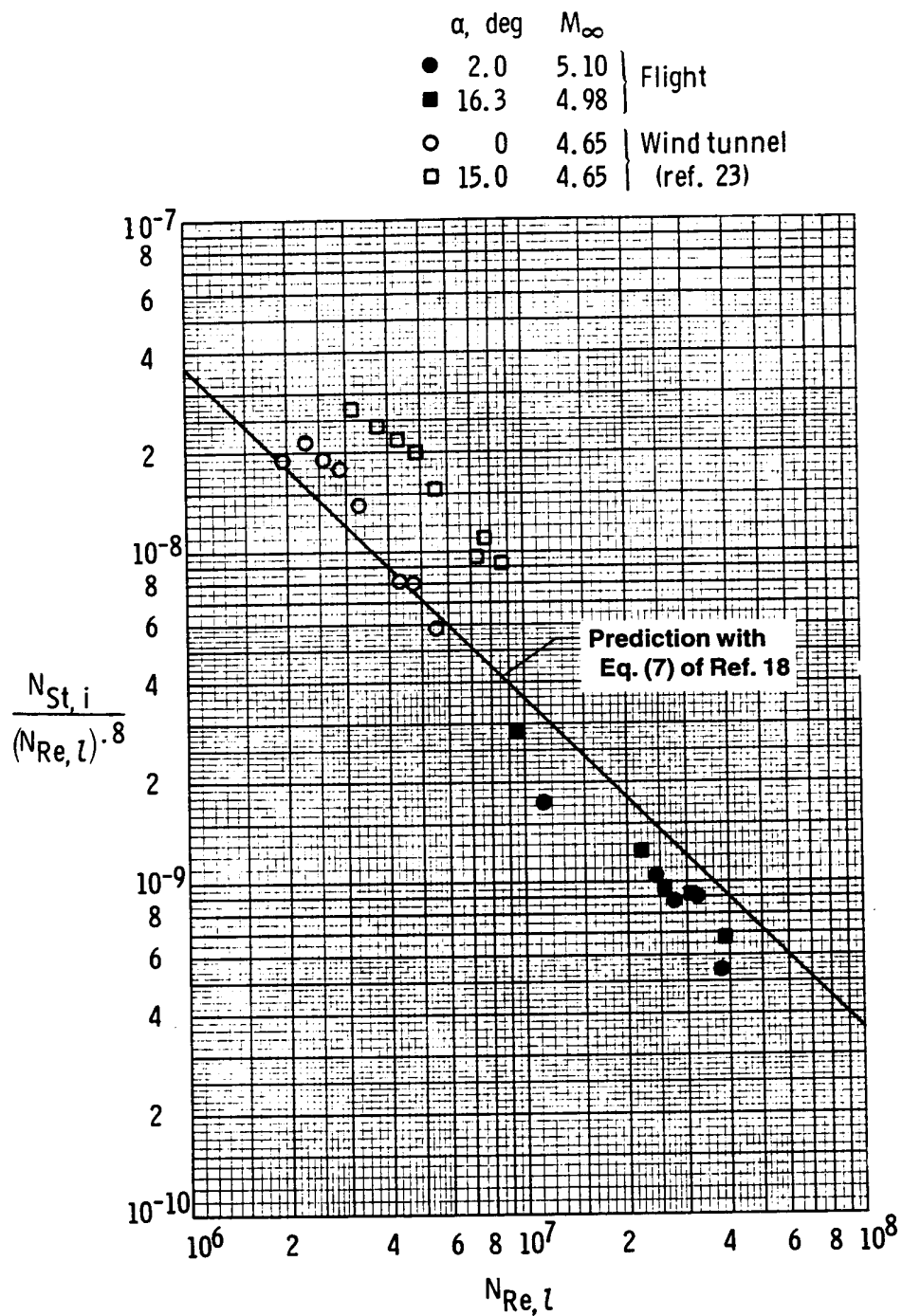


Fig. 6 Damaged windshield glass following flight to $[M_{max}] = 6.04$. (Ref. 22 Fig. 12).



920720

FIG. 7 Reynolds number correlation of wind tunnel and flight data using Eckert's reference enthalpy method, for the lower fuselage of the X-15. (Ref. 18 Fig. 13).

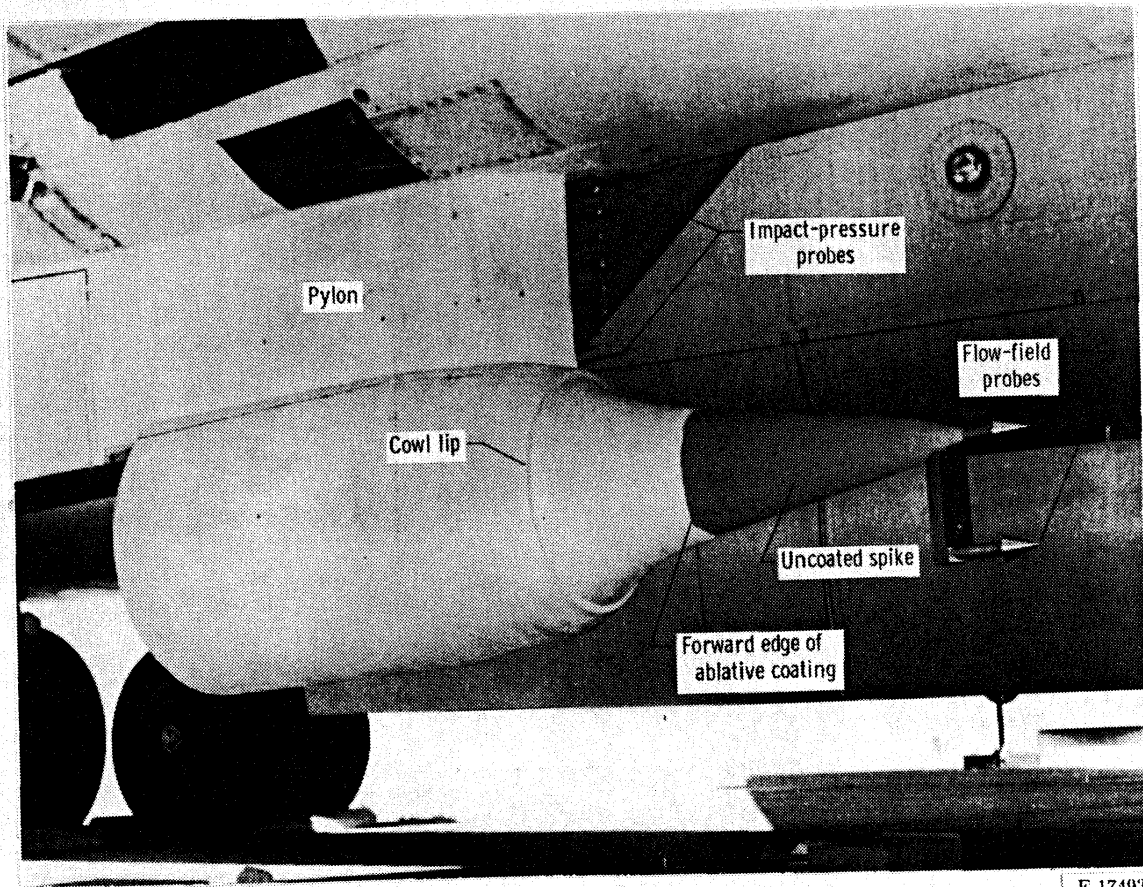
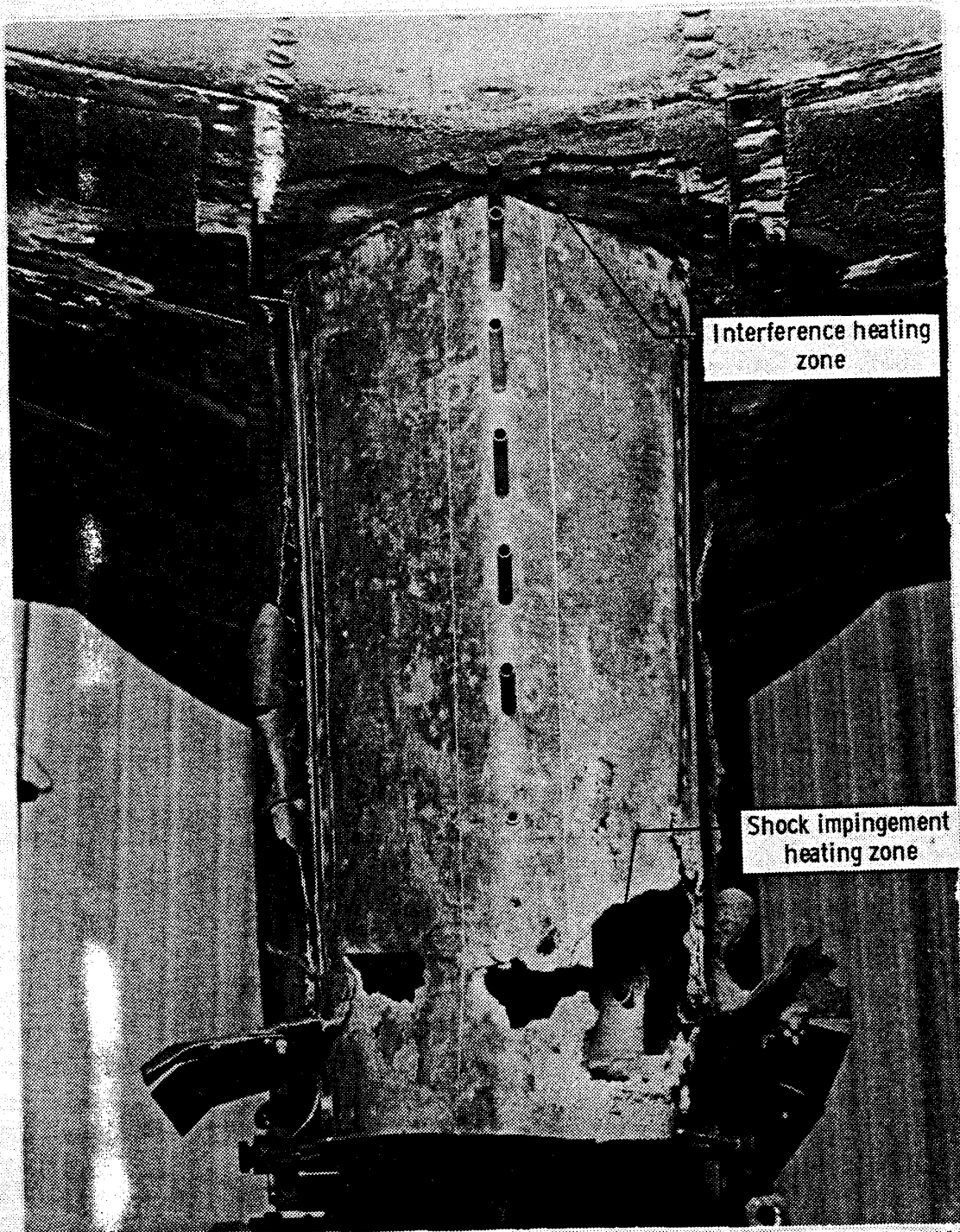


Fig. 8 Pre-flight condition of dummy ramjet engine and pylon. (Ref. 24 Fig. 2).

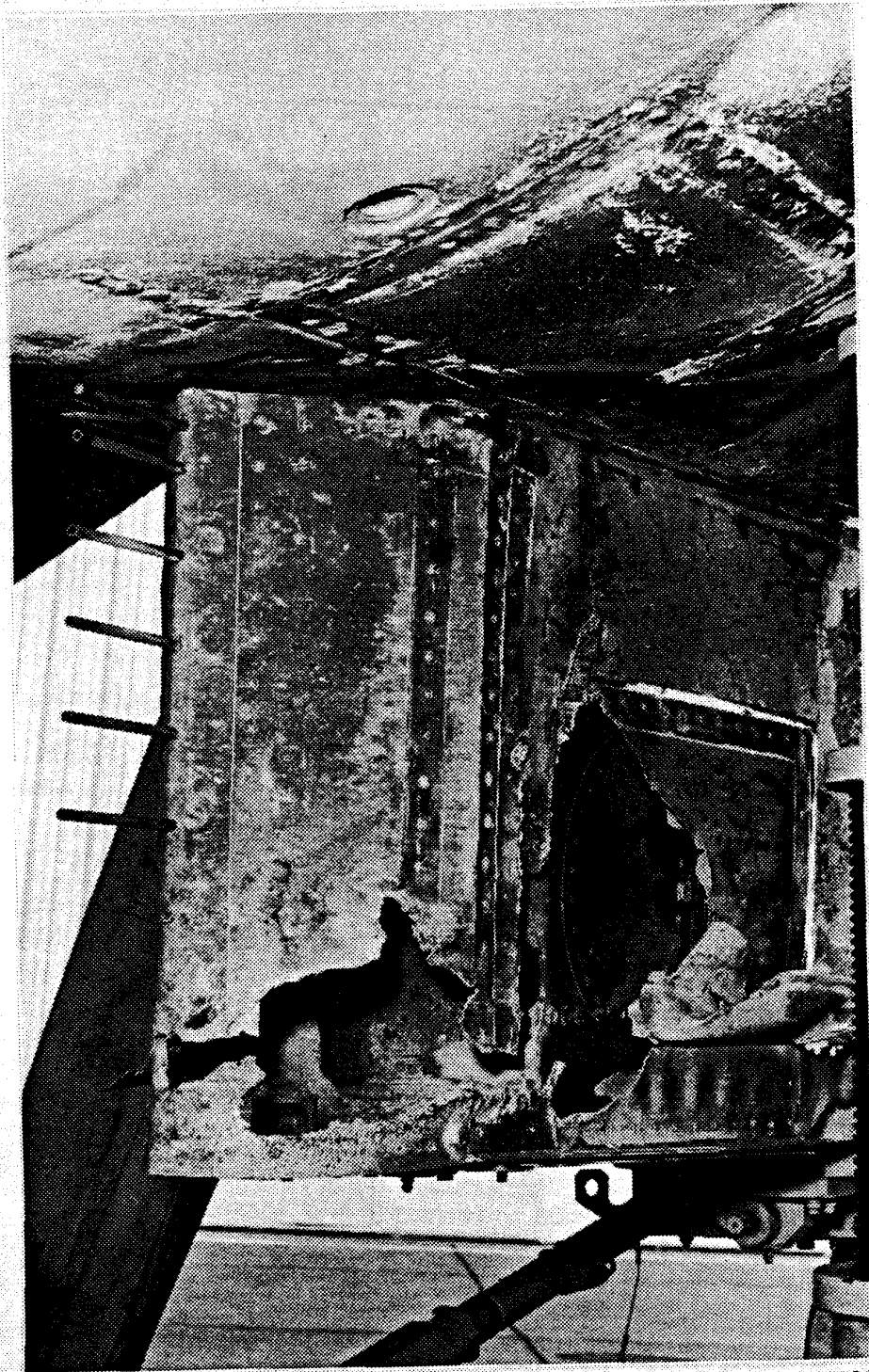
E-17493



E-17525

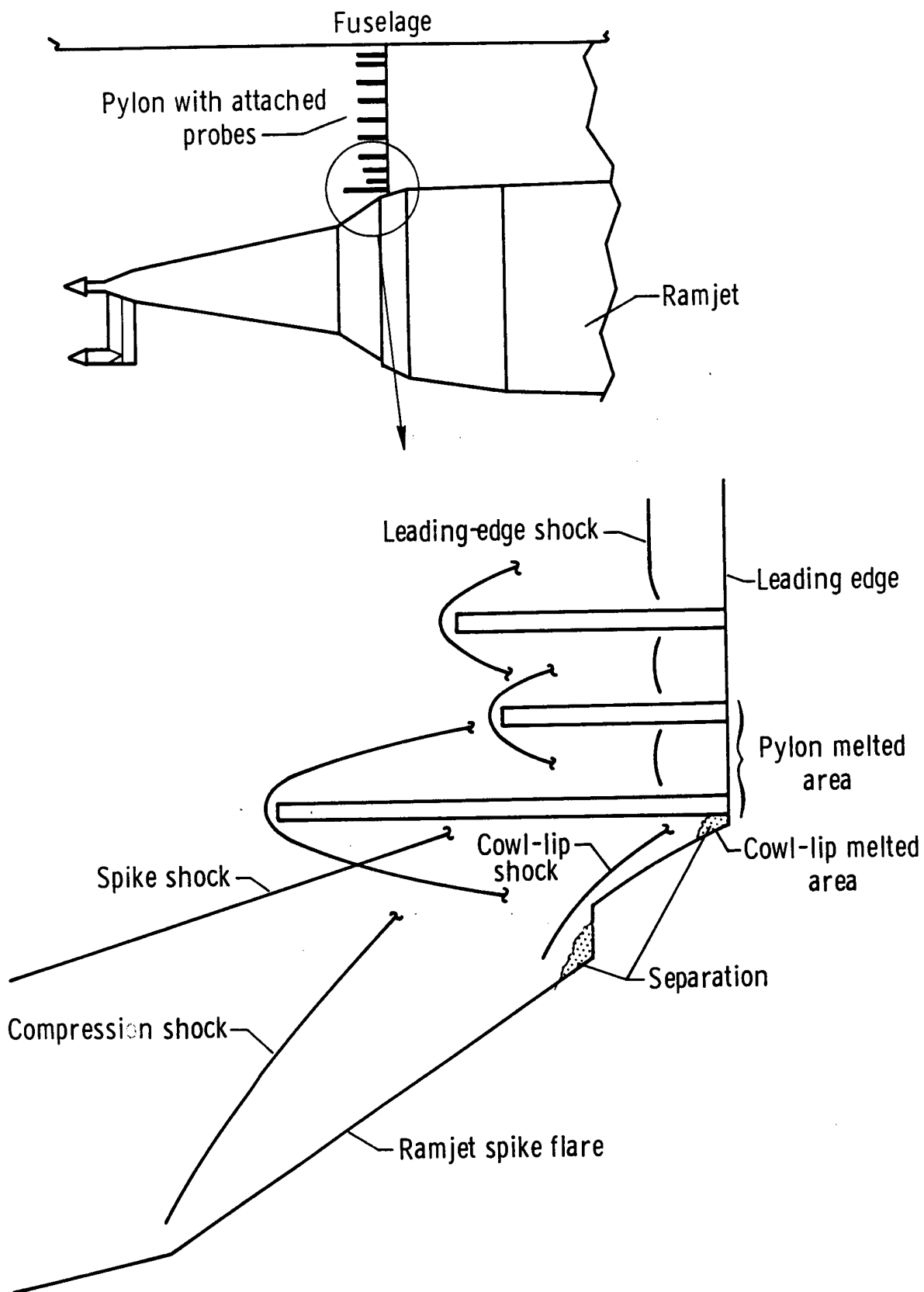
(a) Front view.

Fig. 9 Post-flight condition of dummy ramjet engine and pylon. (Ref. 24 Fig. 7).



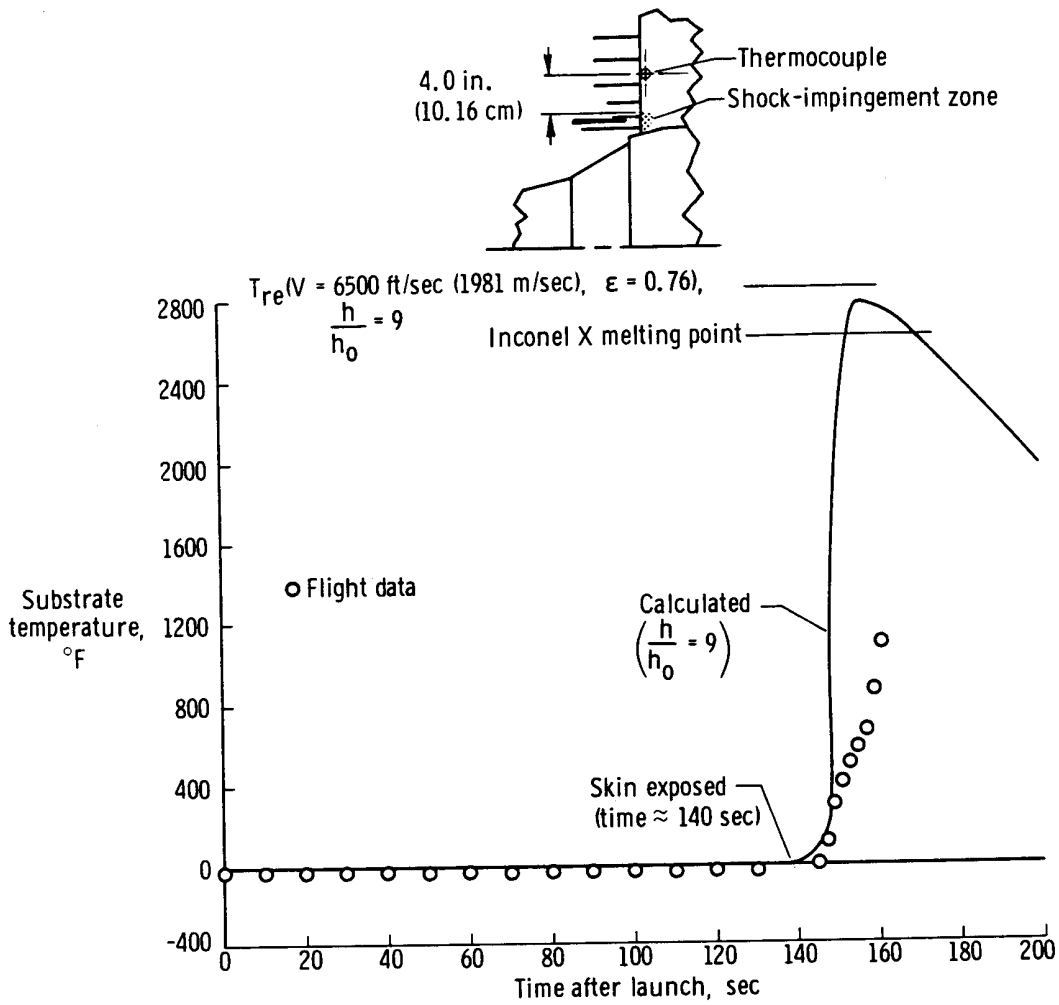
E-17526

(b) Left side view.
Fig. 9 Concluded.



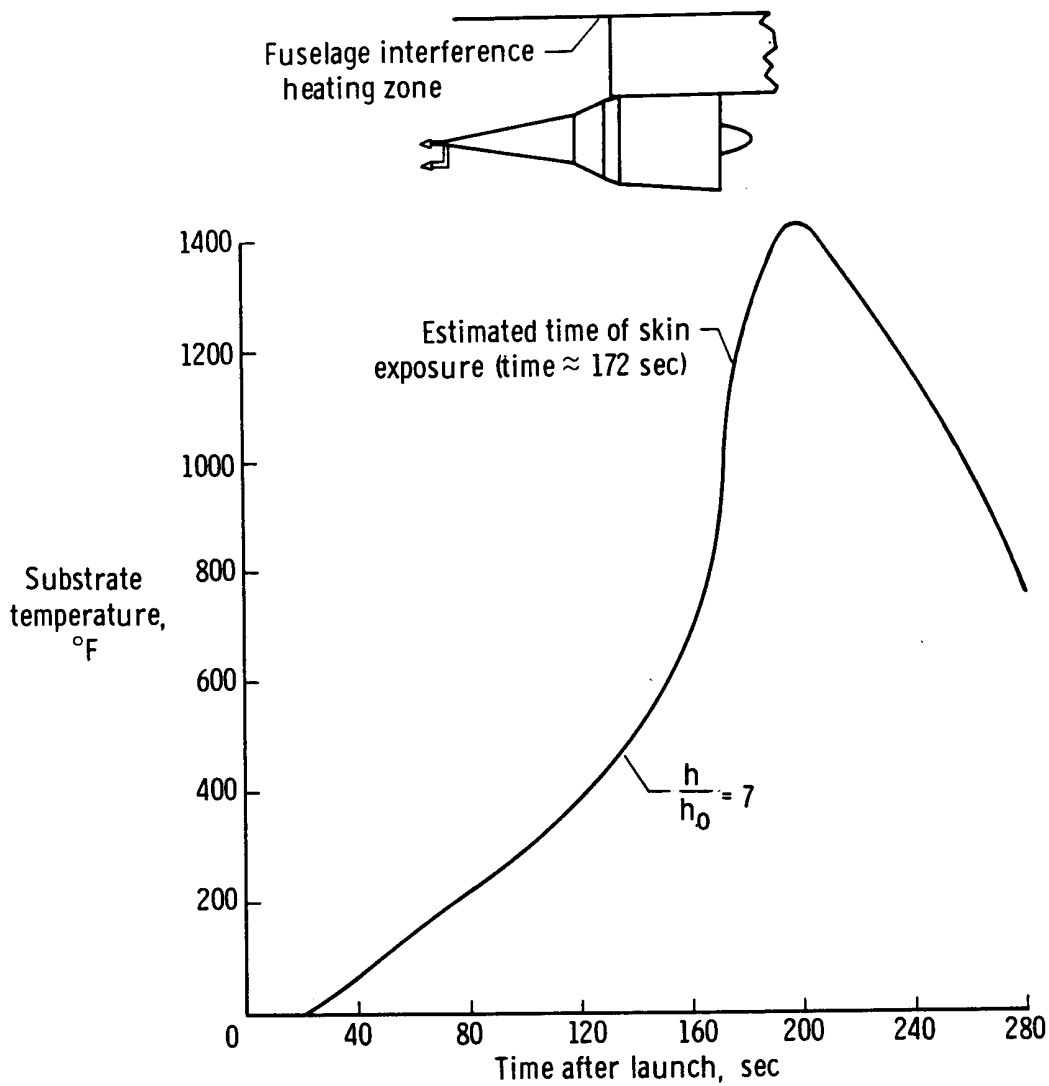
920721

Fig. 10 Assumed shock patterns in shock impingement and cowl-lip interference zones. (Ref. 24 Fig. 9).



920722

Fig. 11 Calculated substrate temperature time history in shock impingement zone compared to nearest measured temperature. (Ref. 24 Fig. 11).



920723

Fig. 12 Calculated substrate temperature time history of fuselage interference heating zone. (Ref. 24 Fig. 11).

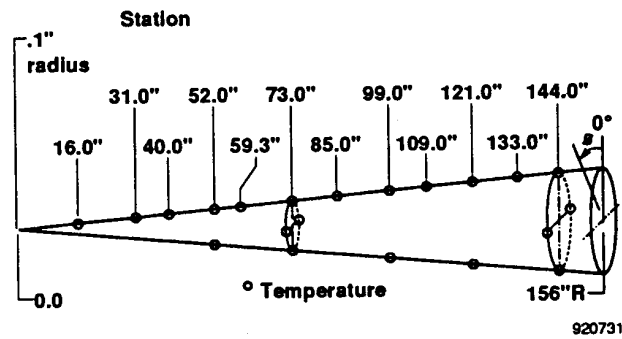


Fig. 13 Temperature measurement locations on Reentry F vehicle. (Ref. 4 Fig. 1).

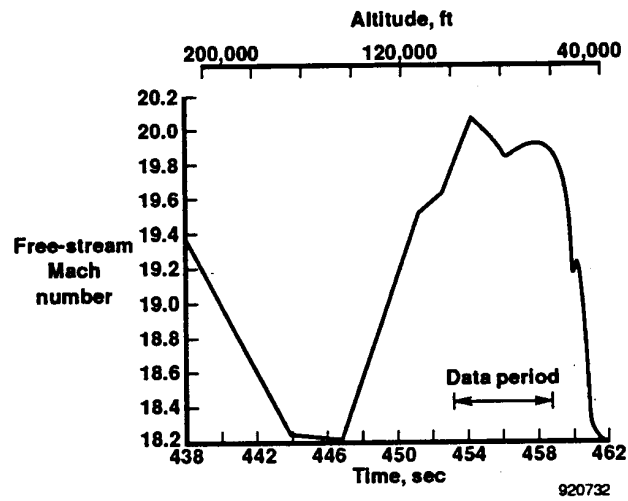


Fig. 14 History of freestream Mach number. (Ref. 4 Fig. 2c).

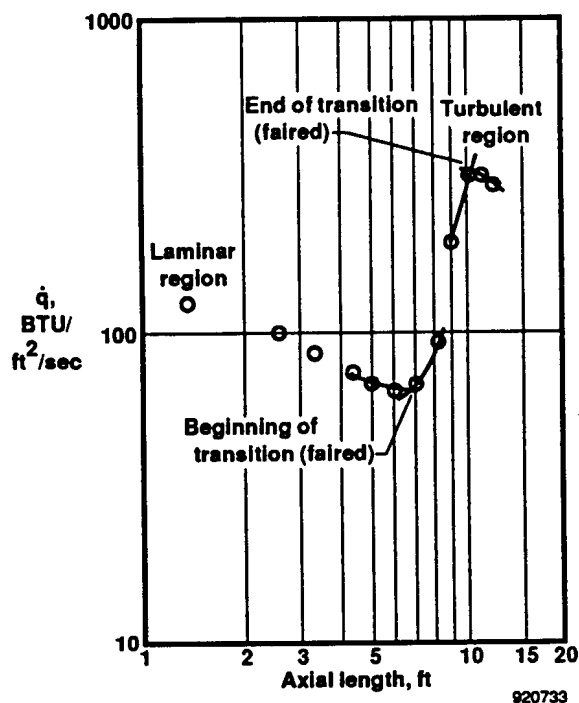


Fig. 15 Transition determination from heating-rate distribution method. (Ref. 4 Fig. 4).

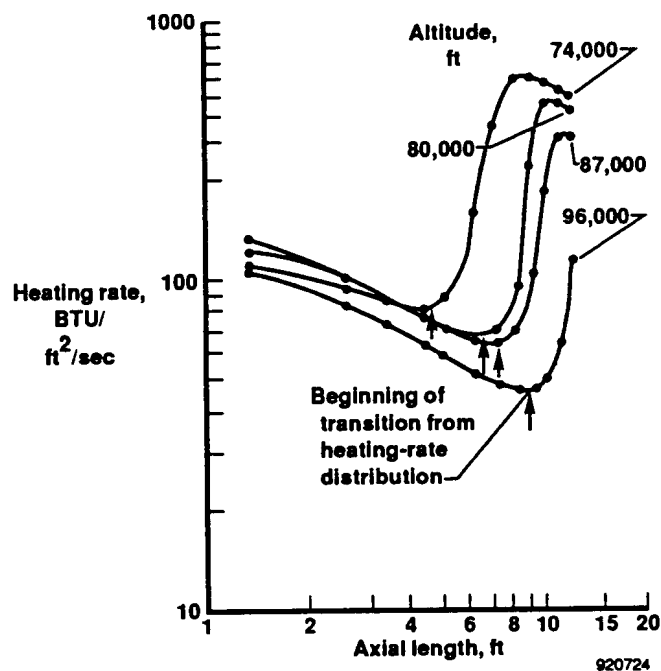


Fig. 16 Comparison of transition locations for a Mach number of 20 at altitudes from 96,000 to 74,000 ft. (Ref. 4 Fig. 8).

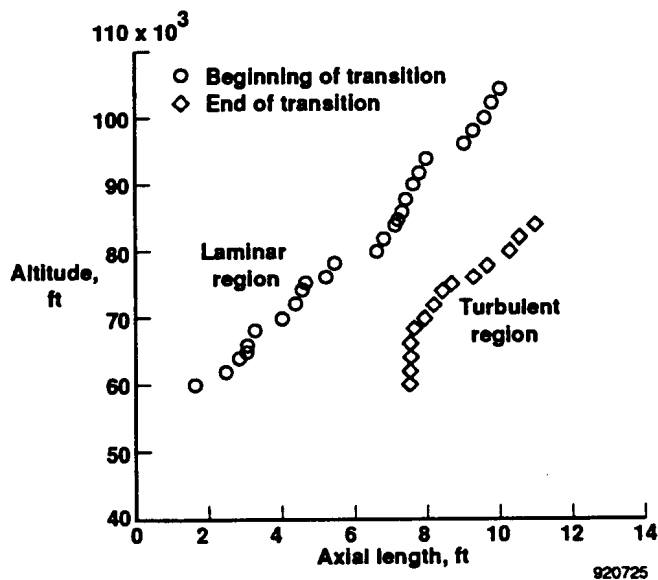


Fig. 17 The relationship of the beginning and end of transition with altitude for Mach = 20. (Ref. 4 Fig. 5).

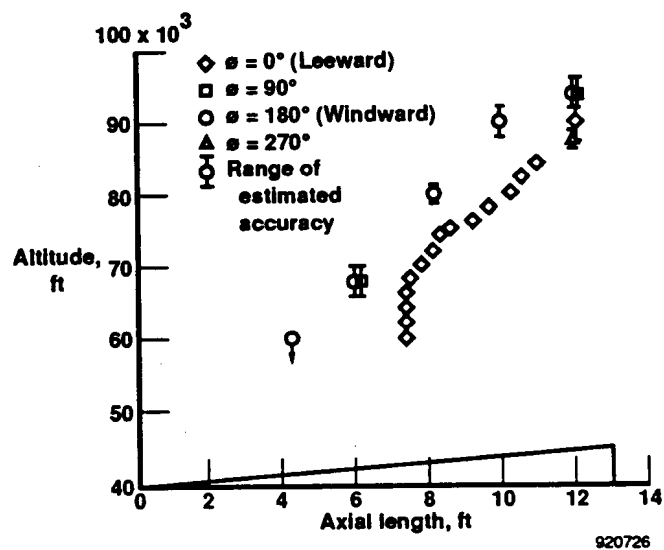


Fig. 18 End of transition location effect for small angles of attack, (axial distribution). (Ref. 4 Fig. 12).

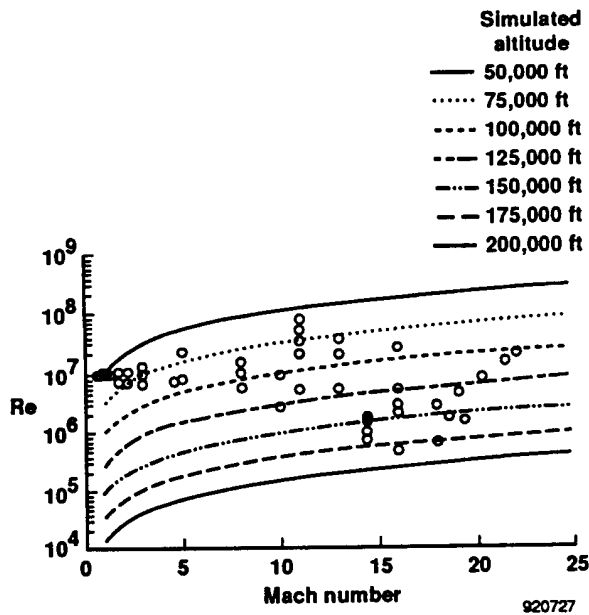


Fig. 19 Wind tunnel test conditions for the SWERVE vehicle.

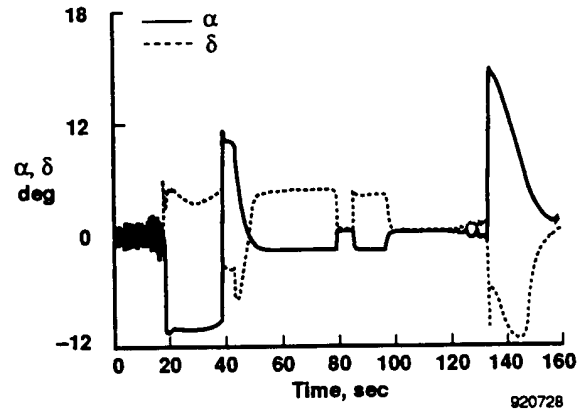


Fig. 20 Angle of attack and control deflection time histories for the SWERVE vehicle.

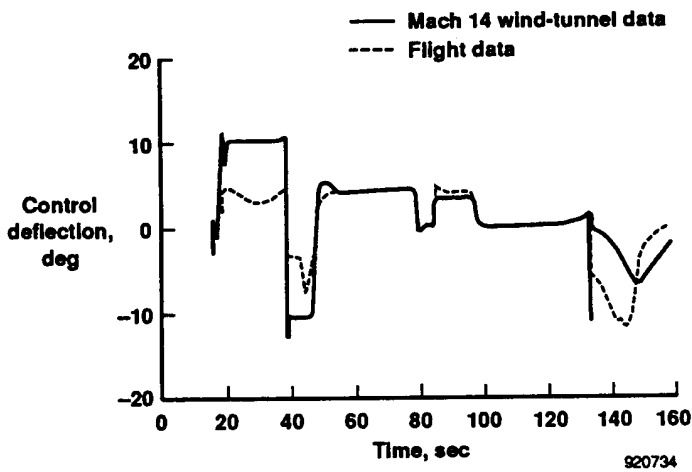


Fig. 21 Comparison of flight measured control deflection with Mach 14 wind tunnel prediction.

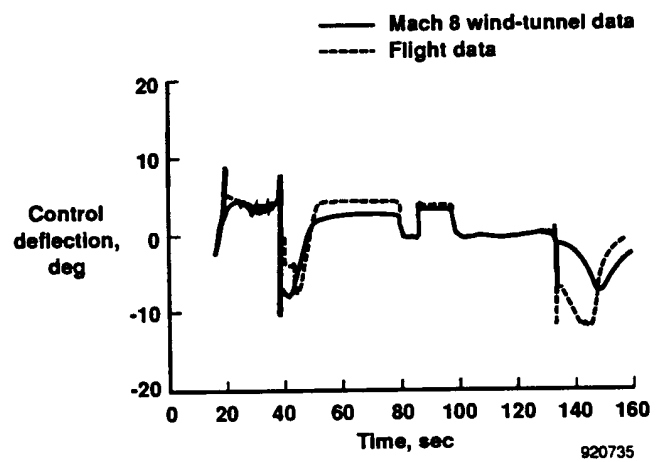


Fig. 22 Comparison of flight measured control deflection with Mach 8 wind tunnel prediction.

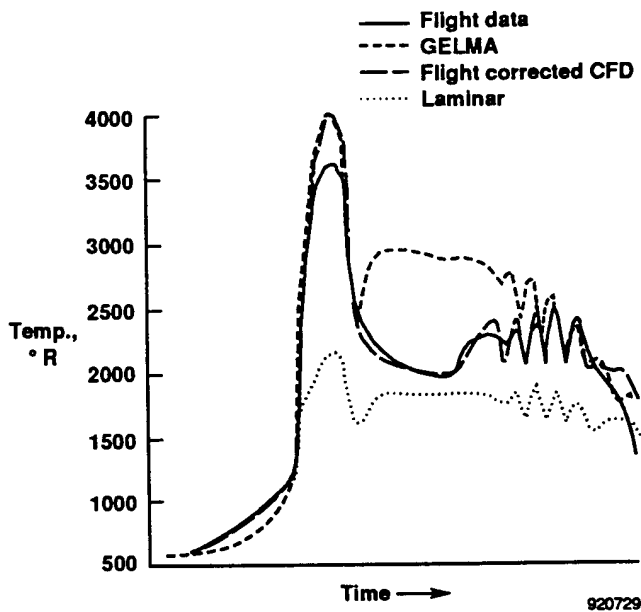


Fig. 23 Comparison of flight measured temperature on the cone with predicted temperature for several different criteria.

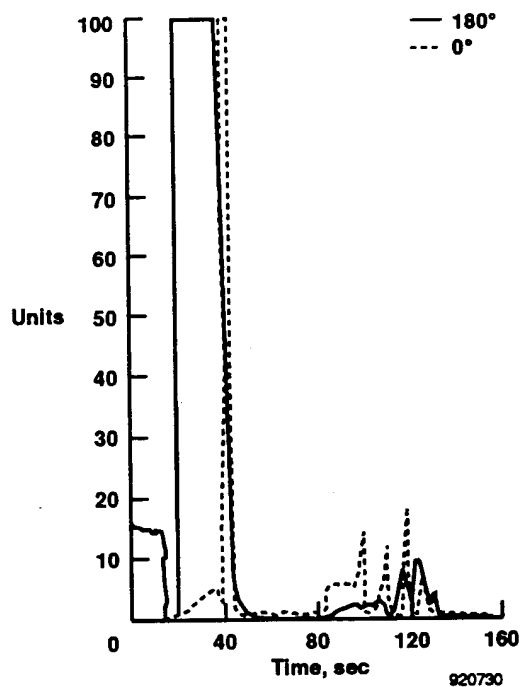


Fig. 24 Photodiode data at 89-in. station for the 180° and the 0° rays.

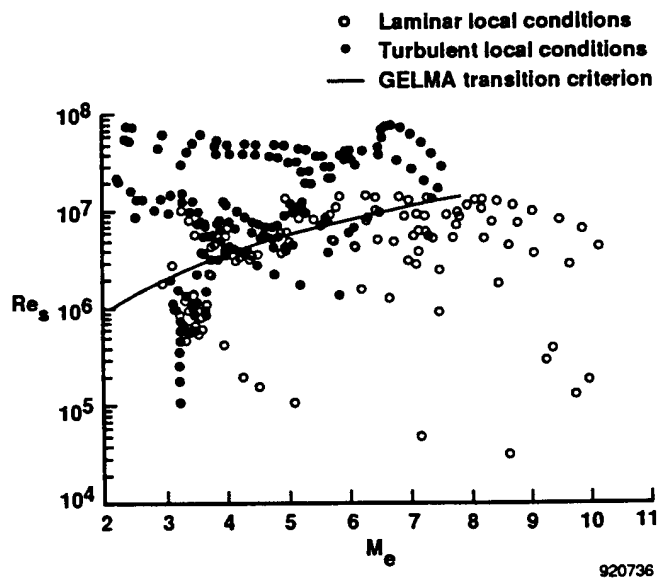


Fig. 25 Comparison of flight data with boundary-layer state and prediction criteria.

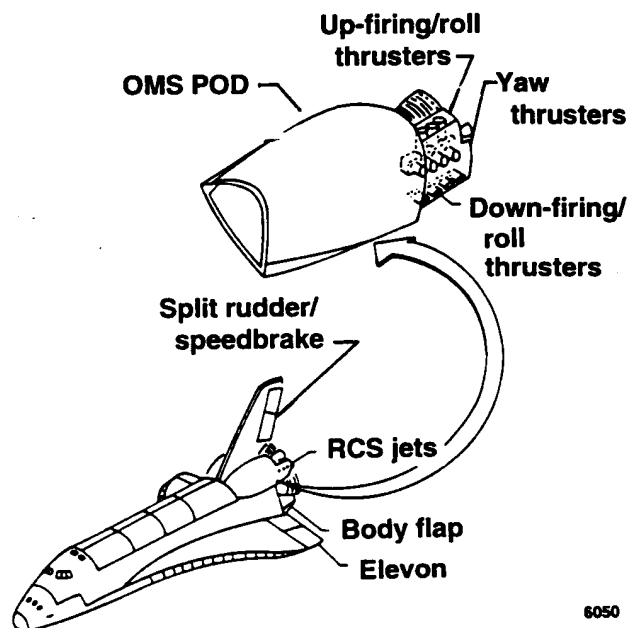


Fig. 26 Space Shuttle configuration. (Ref. 27 Fig. 28).

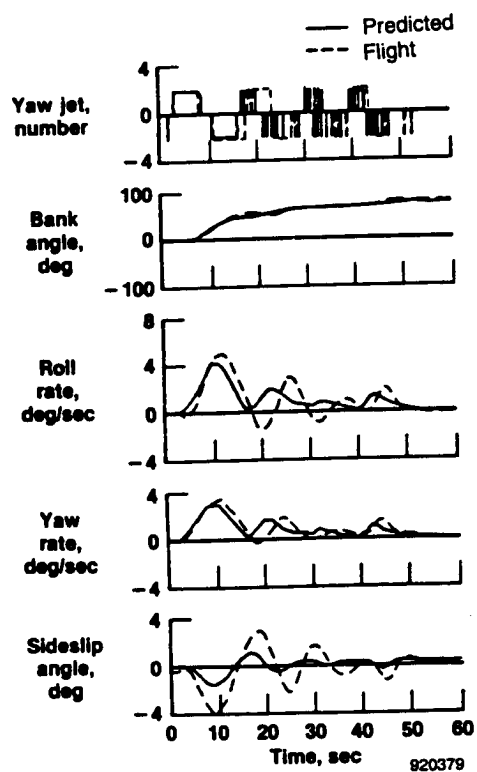


Fig. 27 Comparison of flight (actual) and predicted STS-1 maneuver at Mach 24. (Ref. 27 Fig. 31).

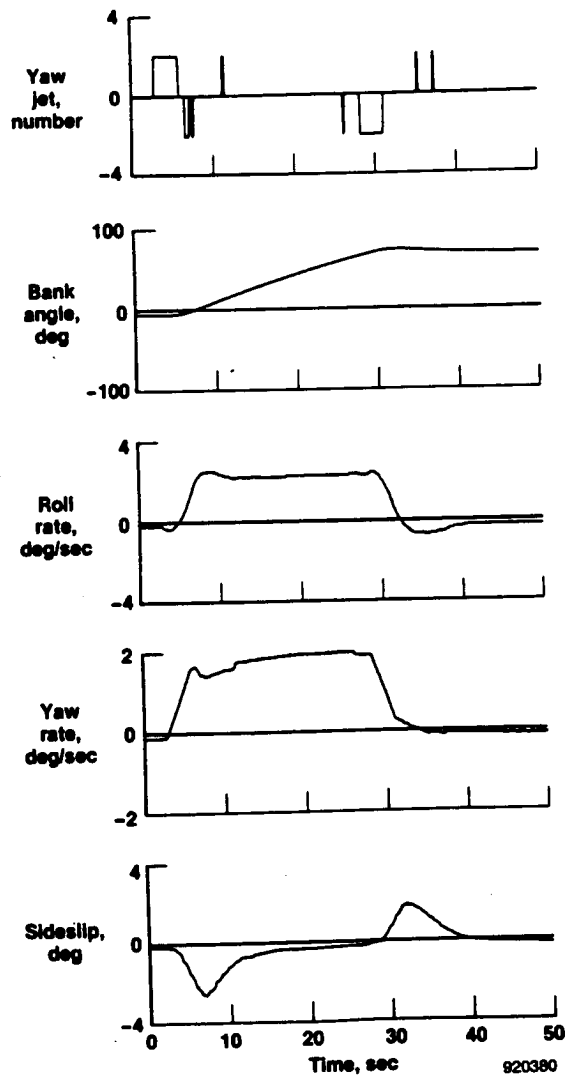


Fig. 28 Manual bank maneuver at $M = 24$ from STS-2. (Ref. 27 Fig. 35).

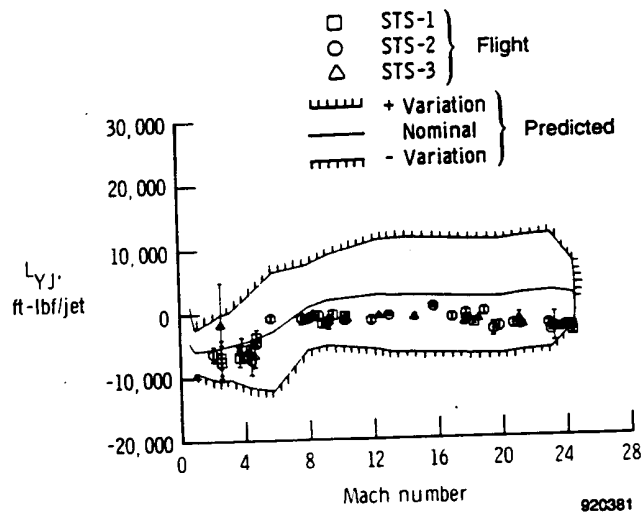


Fig. 29 L_{JY} versus Mach number. (Ref. 28 Fig. 20).

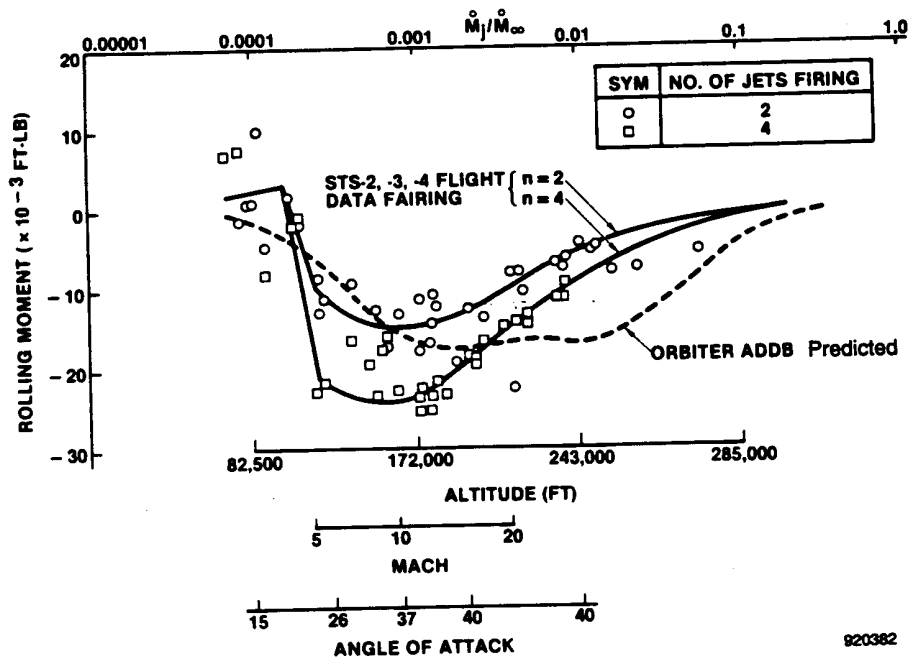


Fig. 30 Yaw jet rolling moment interaction. (Ref. 30 Fig. 2)

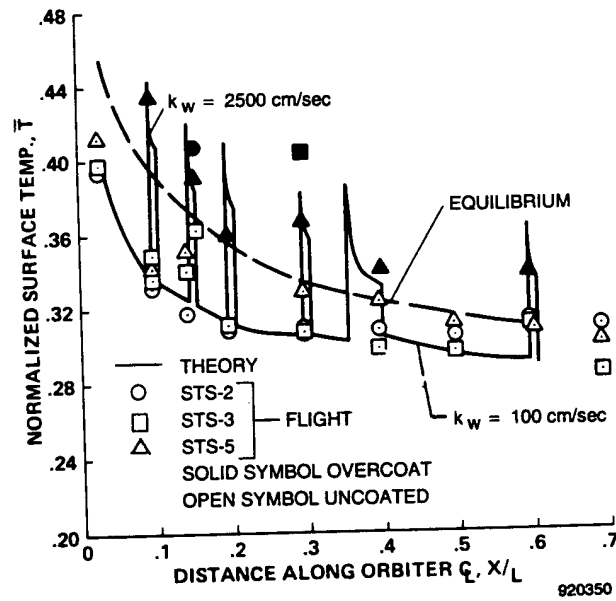


Fig. 31 Surface temperature distribution along midfuselage centerline. (Ref. 33 Fig. 14)

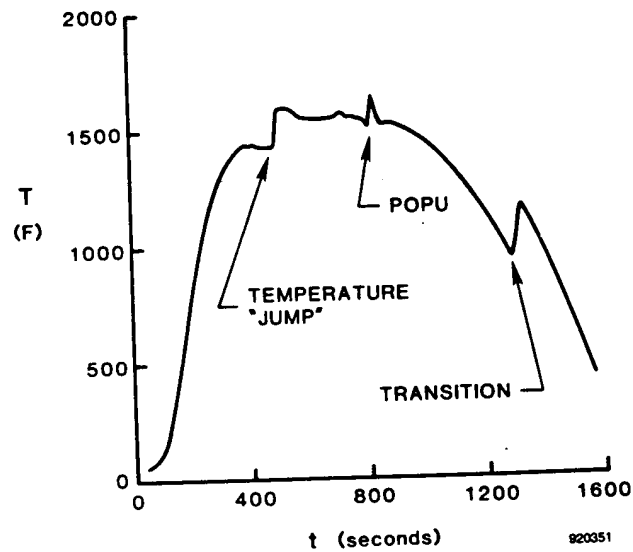


Fig. 32 STS-2 temperature time history at $X/L = 0.194$. (Ref. 34 Fig. 2)

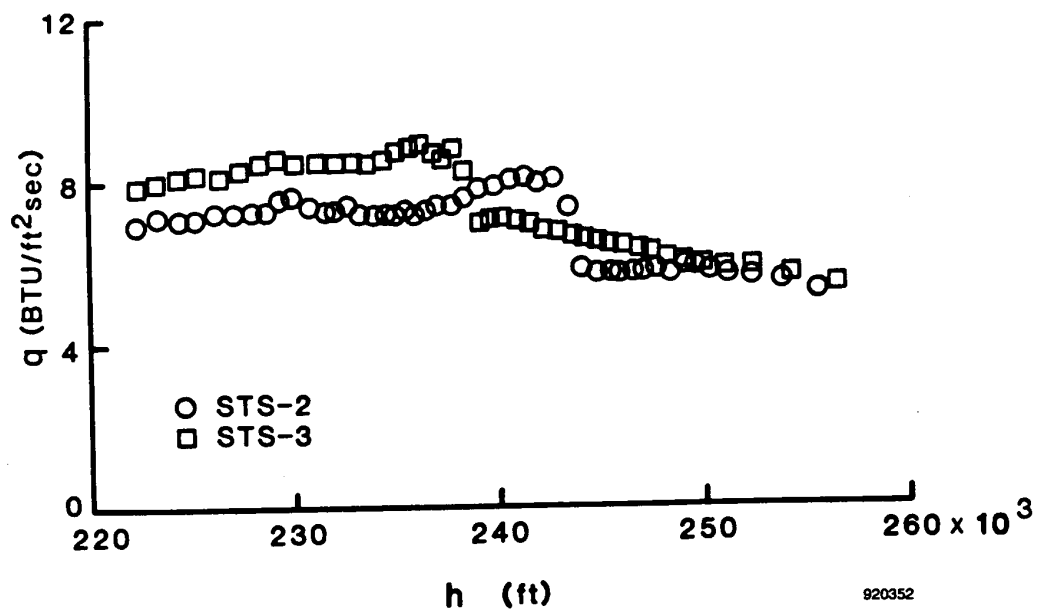


Fig. 33 Heat transfer to tile on flights STS-2 and STS-3 at $X/L = 0.194$. (Ref. 34 Fig. 7)

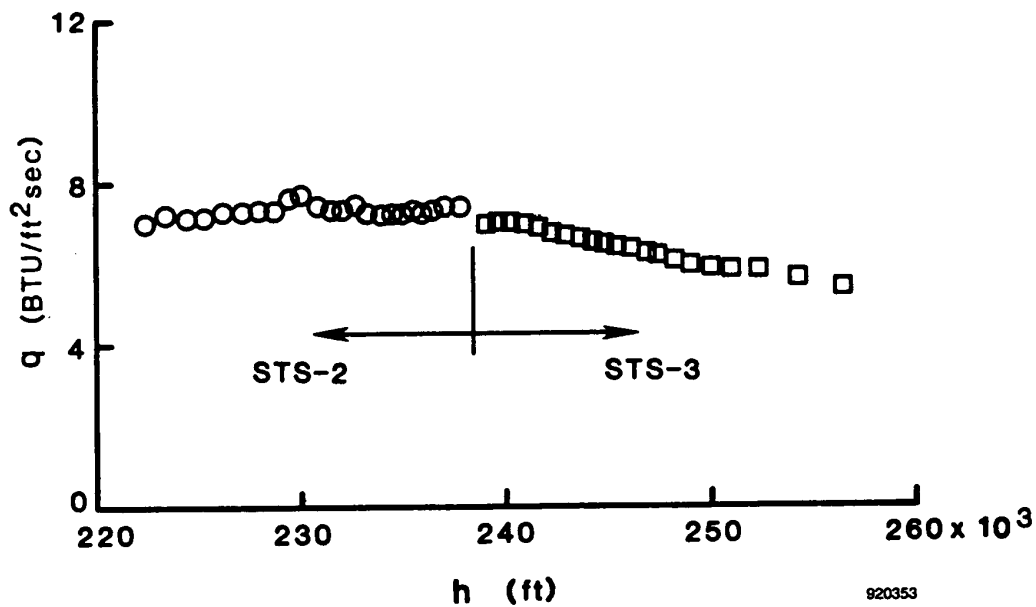


Fig. 34 Heat transfer to tile before and after contamination in flight at $X/L = 0.194$. (Ref. 34 Fig. 8)

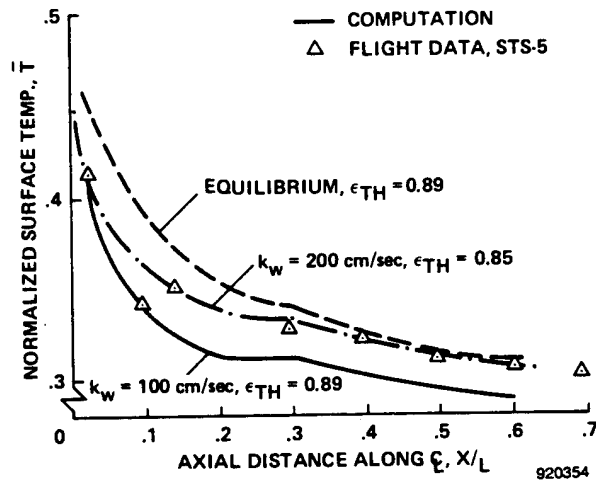


Fig. 35 Comparison of measured and predicted surface temperatures using post-flight STS-5 RCG surface properties at $M_\infty/\sqrt{R_\infty} = 0.0304$. (Ref. 33 Fig. 15)

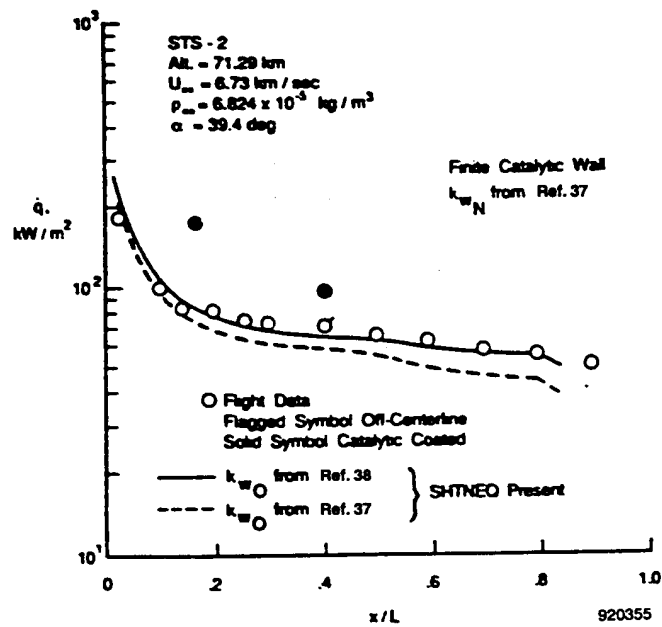


Fig. 36 Nonequilibrium heat-transfer prediction along the windward centerline at an altitude of 75 km. (Ref. 36 Fig. 4).

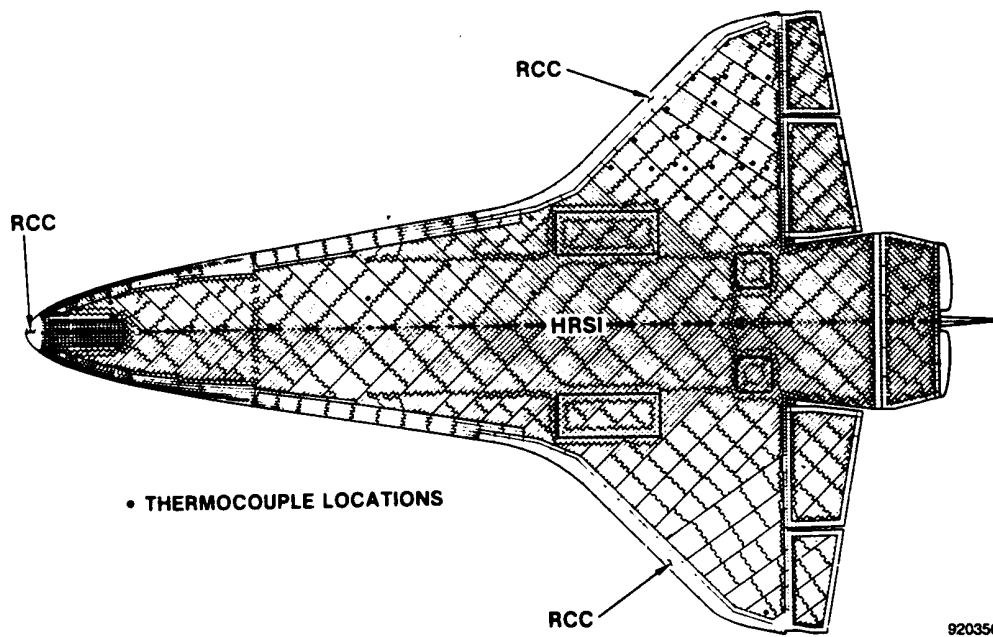


Fig. 37 Orbiter lower surface tile pattern and surface thermocouple layout. (Ref. 39 Fig. 1

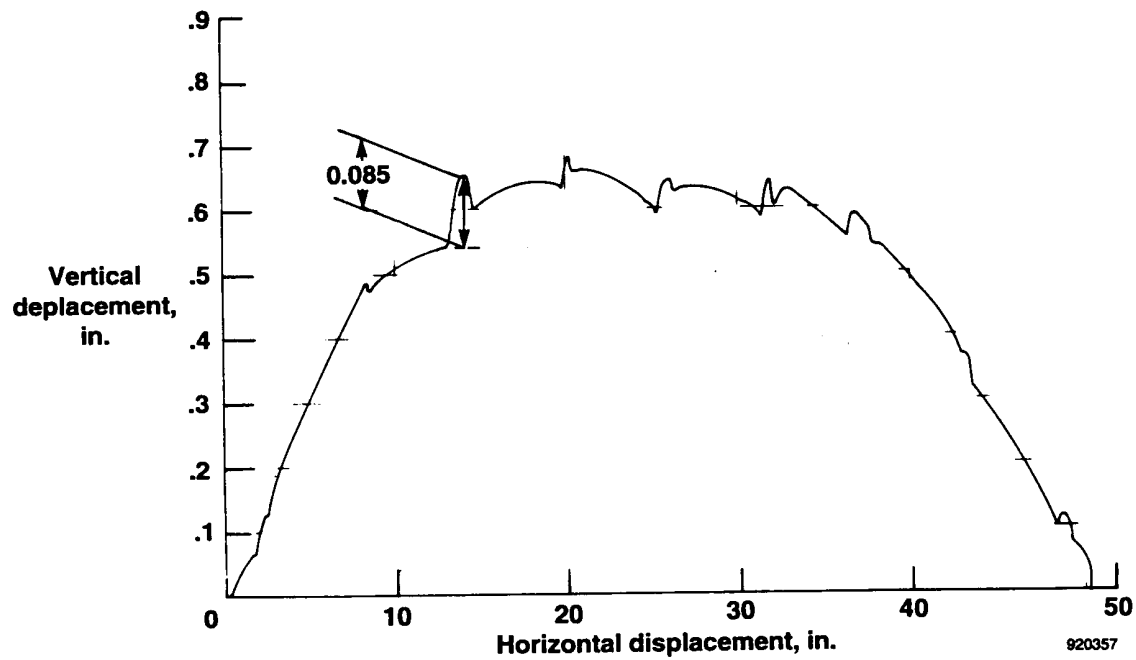


Fig. 38 TPS tile profilometer trace (landing gear door). (Ref. 39 Fig. 2

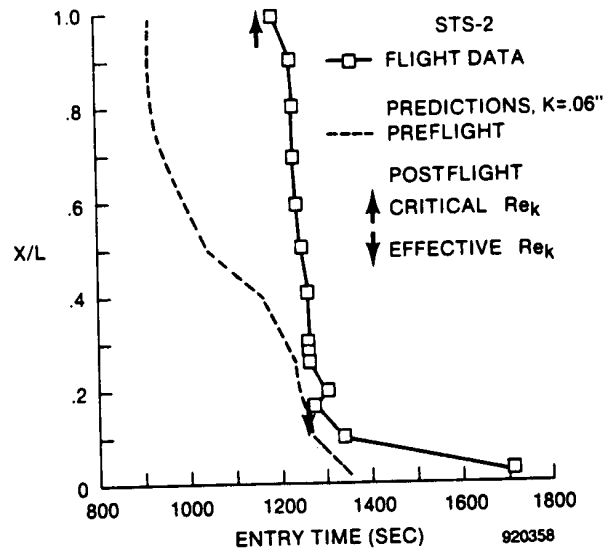


Fig. 39 Comparison of predicted and measured transition times for STS-2. (Ref. 40 Fig. 12b)

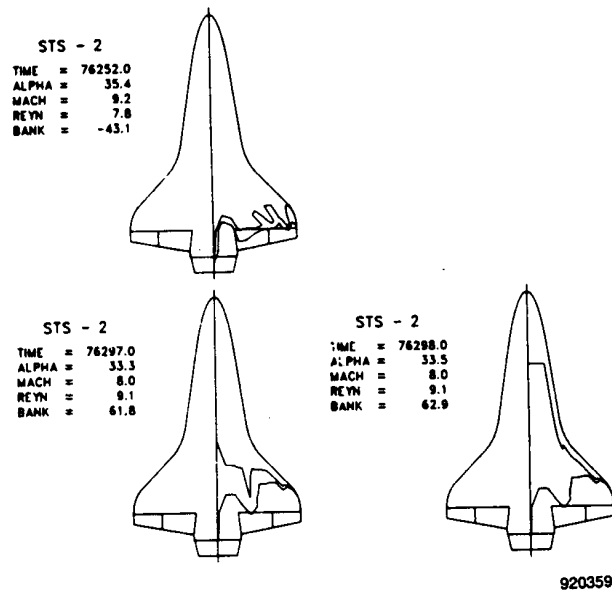


Fig. 40 Three STS-2 transition contour plots for windward surface. (Ref. 41 Fig. 8).

TEMPERATURE, DEG F

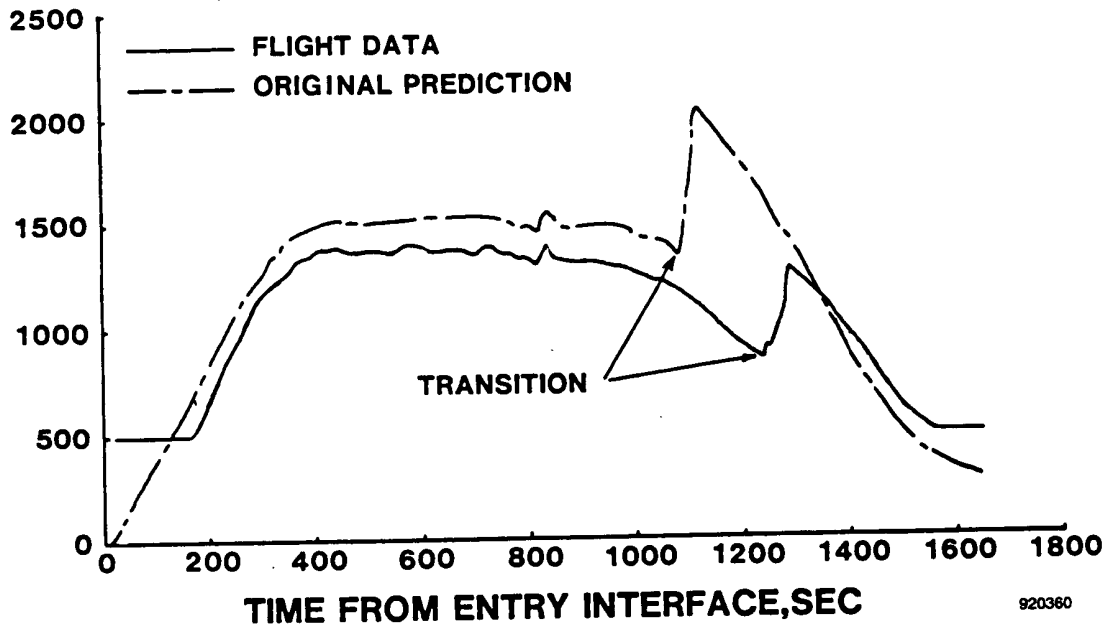


Fig. 41 Lower surface temperature comparison at $X/L = 0.7$. (Ref. 42 Fig. 6)

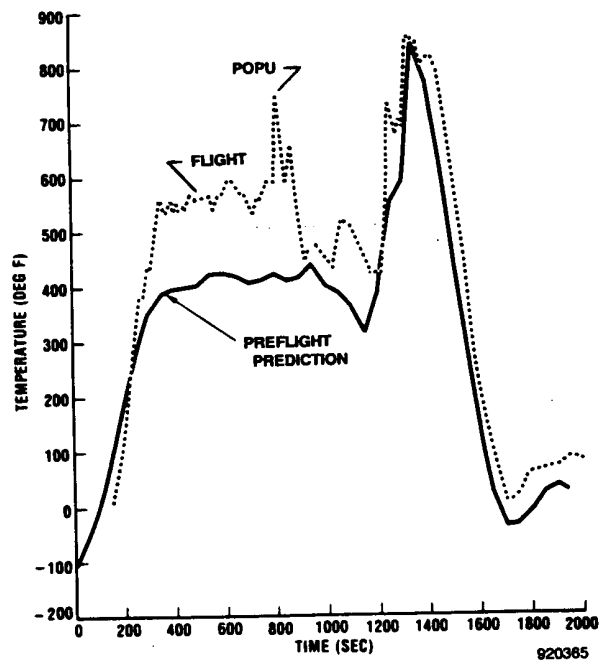


Fig. 42 STS-2 OMS pod temperature profiles. (Ref. 43 Fig. 26)

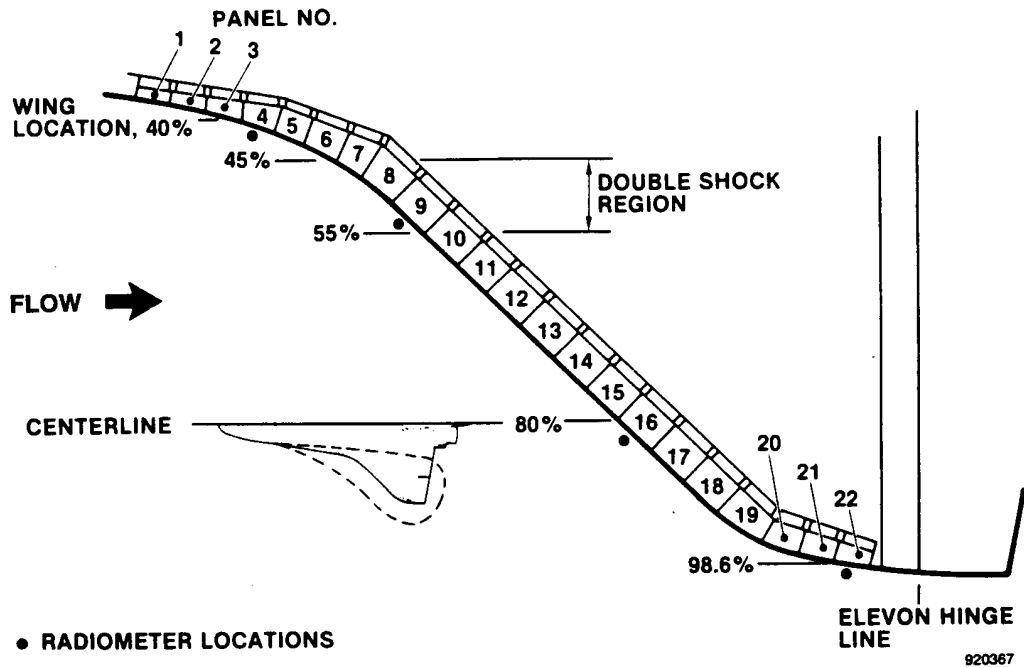


Fig. 43 Orbiter radiometer locations. (Ref. 44 Fig. 6)

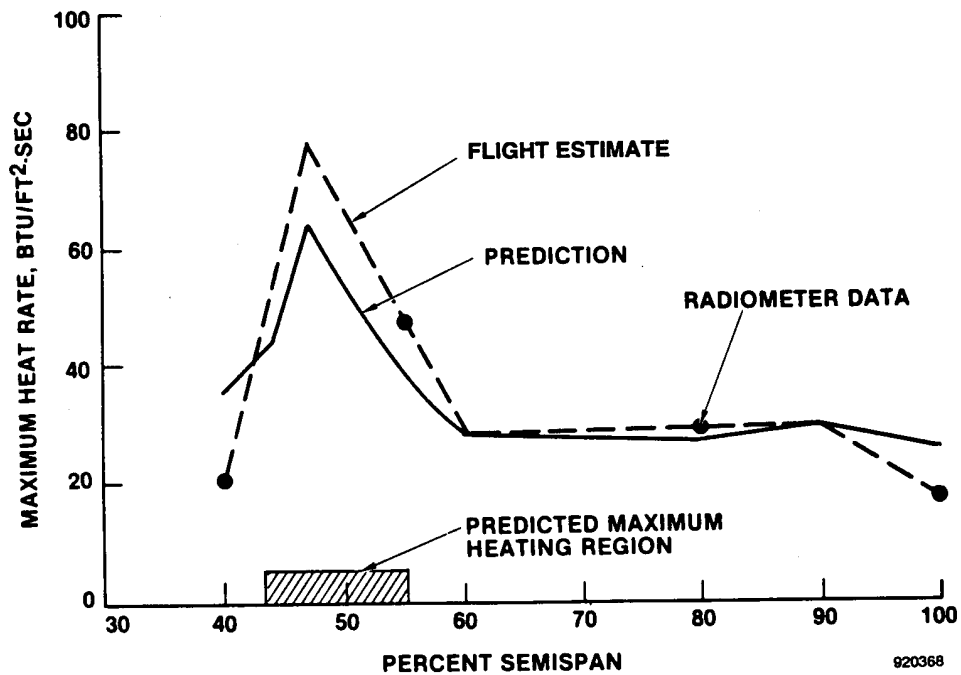


Fig. 44 Spanwise leading-edge maximum heat rate comparison. (Ref. 44 Fig. 11)

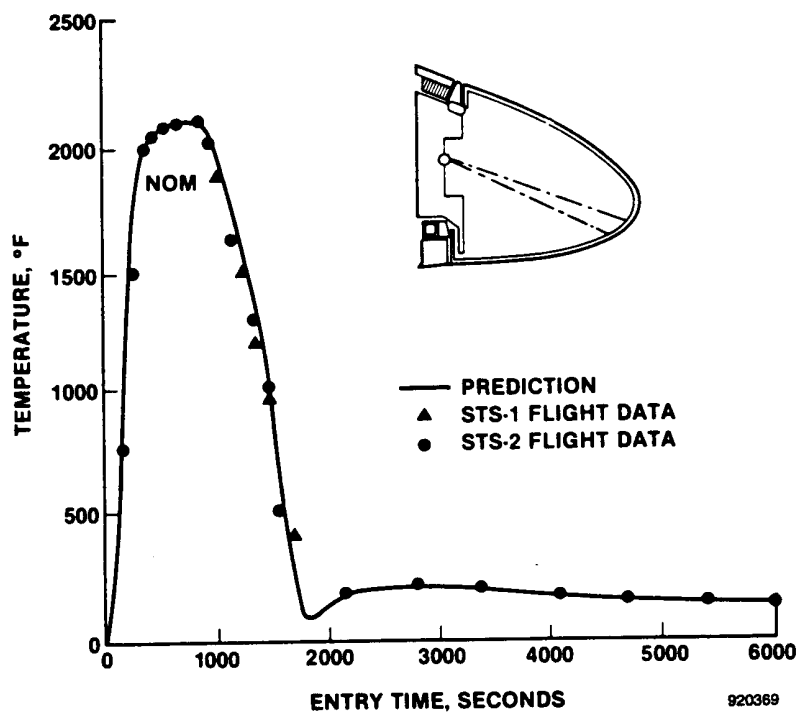


Fig. 45 80-percent semispan leading-edge data comparison to prediction. (Ref. 44 Fig. 9)

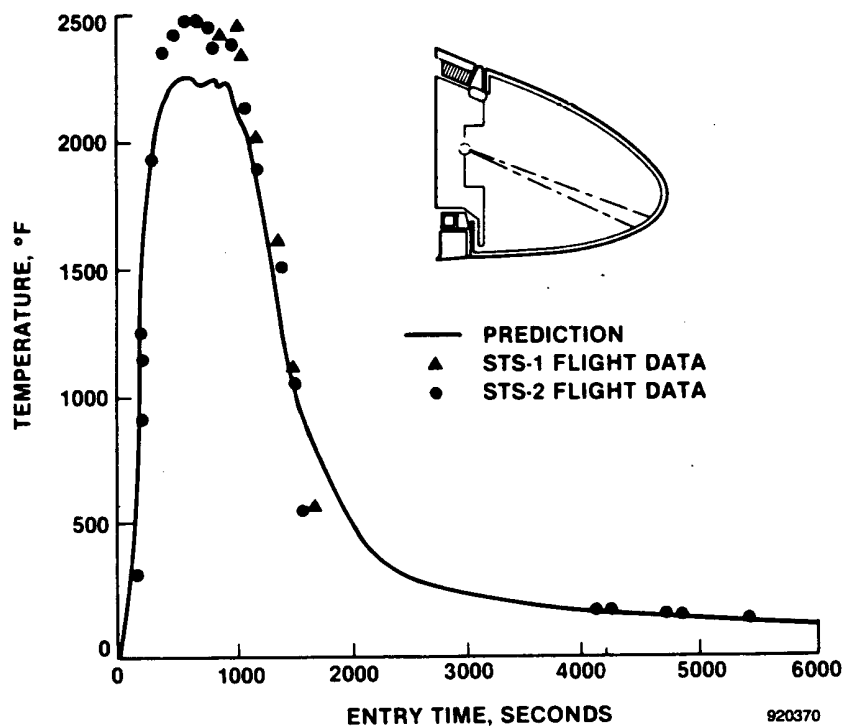


Fig. 46 55-percent semispan leading-edge data comparison to prediction. (Ref. 44 Fig. 8)

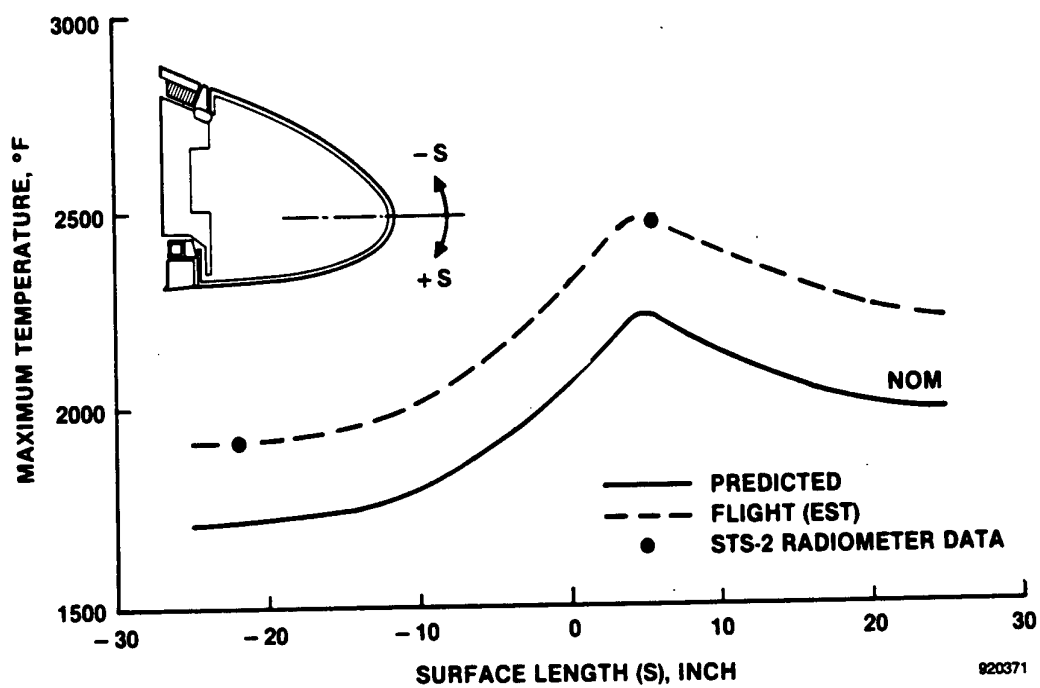


Fig. 47 55-percent semispan leading-edge temperature distribution. (Ref. 44 Fig. 10)

REPORT DOCUMENTATION PAGE			Form Approved OMB No. 0704-0188	
Public reporting burden for this collection of information is estimated to average 1 hour per response, including the time for reviewing instructions, searching existing data sources, gathering and maintaining the data needed, and completing and reviewing the collection of information. Send comments regarding this burden estimate or any other aspect of this collection of information, including suggestions for reducing this burden, to Washington Headquarters Services, Directorate for Information Operations and Reports, 1215 Jefferson Davis Highway, Suite 1204, Arlington, VA 22202-4302, and to the Office of Management and Budget, Paperwork Reduction Project (0704-0188), Washington, DC 20503.				
1. AGENCY USE ONLY (Leave blank)		2. REPORT DATE October 1995		3. REPORT TYPE AND DATES COVERED Technical Memorandum
4. TITLE AND SUBTITLE A Comparison of Hypersonic Vehicle Flight and Prediction Results			5. FUNDING NUMBERS WU 505-65-50	
6. AUTHOR(S) Kenneth W. Iliff and Mary F. Shafer				
7. PERFORMING ORGANIZATION NAME(S) AND ADDRESS(ES) NASA Dryden Flight Research Center P.O. Box 273 Edwards, California 93523-0273			8. PERFORMING ORGANIZATION REPORT NUMBER H-2074	
9. SPONSORING/MONITORING AGENCY NAME(S) AND ADDRESS(ES) National Aeronautics and Space Administration Washington, DC 20546-0001			10. SPONSORING/MONITORING AGENCY REPORT NUMBER NASA TM-104313	
11. SUPPLEMENTARY NOTES Presented as AIAA 93-0311 at the 31st Aerospace Sciences Meeting and Exhibit, Reno, Nevada, Jan. 11-14, 1993.				
12a. DISTRIBUTION/AVAILABILITY STATEMENT Unclassified—Unlimited Subject Category 34			12b. DISTRIBUTION CODE	
13. ABSTRACT (Maximum 200 words) Aerodynamic and aerothermodynamic comparisons between flight and ground test for four hypersonic vehicles are discussed. The four vehicles are the X-15, the Reentry F, the Sandia Energetic Reentry Vehicle Experiment (SWERVE), and the Space Shuttle. The comparisons are taken from papers published by researchers active in the various programs. Aerodynamic comparisons include reaction control jet interaction on the Space Shuttle. Various forms of heating including catalytic, boundary layer, shock interaction and interference, and vortex impingement are compared. Predictions were significantly exceeded for the heating caused by vortex impingement (on the Space Shuttle OMS pods) and for heating caused by shock interaction and interference on the X-15 and the Space Shuttle. Predictions of boundary-layer state were in error on the X-15, the SWERVE, and the Space Shuttle vehicles.				
14. SUBJECT TERMS Aerothermodynamics; Boundary-layer transition; Catalytic effects; Flight-to-ground test correlation; Hypersonic aerodynamics; Shuttle reentry; X-15 aircraft			15. NUMBER OF PAGES 45	
			16. PRICE CODE AO4	
17. SECURITY CLASSIFICATION OF REPORT Unclassified	18. SECURITY CLASSIFICATION OF THIS PAGE Unclassified	19. SECURITY CLASSIFICATION OF ABSTRACT Unclassified	20. LIMITATION OF ABSTRACT Unlimited	